

# Fluid-Filled Fracture Propagation With a Phase-Field Approach and Coupling to a Reservoir Simulator

Thomas Wick, Gurpreet Singh, and Mary F. Wheeler, University of Texas at Austin

## Summary

A quantitative assessment of hydraulic-fracturing jobs relies on accurate predictions of fracture growth during slickwater injection for single and multistage fracturing scenarios. This requires consistent modeling of underlying physical processes, from hydraulic fracturing to long-term production. In this work, we use a recently introduced phase-field approach to model fracture propagation in a porous medium. This approach is thermodynamically consistent and captures several characteristic features of crack propagation such as joining, branching, and nonplanar propagation as a result of heterogeneous material properties. We describe two different phase-field fracture-propagation models and then present a technique for coupling these to a fractured-poroelastic-reservoir simulator. The proposed coupling approach can be adapted to existing reservoir simulators. We present 2D and 3D numerical tests to benchmark, compare, and demonstrate the predictive capabilities of the fracture-propagation model as well as the proposed coupling scheme.

## Introduction

Tight gas and shale oil play an important role in energy security and in meeting an increasing energy demand. Hydraulic fracturing is a widely used technology for recovering these resources. Also, there are concerns regarding the long- and short-term environmental implications of hydraulic-fracturing practices. Thus, there is an imminent need for physically and mathematically consistent, accurate, and robust computational models for representing fractures driven by injected fluids in a poroelastic medium. The simplest model description involves coupling of (1) mechanical deformation, (2) reservoir/fracture fluid flow, and (3) fracture propagation. The rock deformation is usually modeled with the linear elasticity theory (Biot 1941a, b; 1955). For fluid-flow modeling, lubrication theory and Darcy flow are assumed in the fracture and reservoir, respectively, which are coupled through a leakage term. Finally, for fracture propagation, the conventional energy-release rate approach of linear-elastic-fracture-mechanics (LEFM) theory is used. A vast literature is available on a number of concurring modeling and numerical approaches for fracture propagation currently used such as cohesive-zone (CZ) models (Xu and Needleman 1994), displacement-discontinuity methods (DDMs) (Crouch 1976), partition-of-unity (Babuska and Melenk 1997) -based extended/generalized finite-element (XFEM/GFEM) methods (Moes et al. 1999; de Borst et al. 2006; Secchi and Schrefler 2012; Babuska and Banerjee 2012), boundary-element (BEM) formulations, (Castonguay et al. 2013), and peridynamics (Silling 2000).

A number of these approaches were successfully applied to hydraulic-fracturing scenarios. Here, the CZ-finite-element method (CZ-FEM) was used by Chen et al. (2009) whereas DDMs were used by Zhang et al. (2007); Olson (2008); and Peirce and Detournay (2008). Recent findings with XFEM/GFEM methods were reported by Gupta and Duarte (2014) but also in earlier studies by Taleghani (2009); Ren et al. (2009); Lecampion (2009); and Gorde-

liy and Peirce (2013a, b). A peridynamics-based approach for hydraulic fracturing was considered by Katiyar et al. (2014). Finally, asymptotic solutions assuming symmetry in the half-space for penny-shaped fluid-filled fractures were constructed by Zhang et al. (2002) and also by Savitski and Detournay (2002). Kresse et al. (2013) and Meyer and Bazan (2011) investigated fracture growth in a reservoir with a complex network or discrete natural fractures. Further studies with emphasis on field applications and engineering technologies were presented by Abass et al. (2009); Fisher et al. (2004); Germanovich et al. (1997); Roussel and Sharma (2011); Roussel et al. (2012); and Sestetty and Ghassemi (2013).

A variational approach (Francfort and Marigo 1998; Bourdin et al. 2008) for fracture growth in nonporous, solid mechanics was used in the past. Miehe et al. (2010) further extended this variational approach by modeling crack irreversibility as an entropy condition, thereby satisfying the second law of thermodynamics. In addition, the strain tensor is decomposed into two parts to account for tension and compression separately.

However, most of the aforementioned published studies address fracture propagation in an elastic medium (i.e., Biot coefficient  $\alpha=0$ ). For example, Bourdin et al. (2012) formulated phase field in elasticity for hydraulic cracks. However, hydraulic fracturing allows recovery of hydrocarbons from pore volumes of unconventional reservoirs. It is therefore important to account for the poroelastic nature of the reservoir rock in crack-propagation models and to study its consequent effects on fracture growth. Our approach (Mikelić et al. 2013, 2015b) is based on Miehe et al. (2010) with an extension (Mikelić et al. 2015a) to porous-media applications in which the porous-rock matrix interacts with fluids both in the reservoir and the fracture. We present a phase-field formulation for fracture growth in a poroelastic medium in which geomechanics and fluid flow are decoupled with a fixed-stress splitting (Settari and Walters 2001; Dean and Schmidt 2009; Mikelić and Wheeler 2013).

We provide a brief recapitulation describing Griffith's model for fracture growth in brittle media. The classical theorem of minimum energy states that an equilibrium state achieved by an elastic body deformed by surface forces is such that the potential energy of the system is minimal. This was later augmented by Griffith (1921) to account for a different equilibrium state caused by formation of fractures as a mechanism for lowering the potential energy of the system under consideration. This failure criterion assumes that the cohesive forces, caused by molecular attraction, act close to the fracture tip. Thus, one can assume that the contribution of cohesive forces (surface potential energy) to the total potential energy will be negligible. Based on these assumptions, a decrease in potential energy is proportional to the generated surface area with the critical energy-release rate ( $G_c$ ) as the constant of proportionality. In our work, we rely on this classical work along with its assumptions on the fracture-growth criteria. As noted by Barenblatt (1962), we do not underestimate the significance of cohesive forces at the fracture tip. However, the contribution of these forces to the total potential energy is assumed to be significant only during fracture nucleation which diminishes as the fracture grows. Based on these arguments, we assume that LEFM is applicable.

With a phase-field approach, a lower-dimensional crack surface is approximated as a diffusive transition zone, characterized

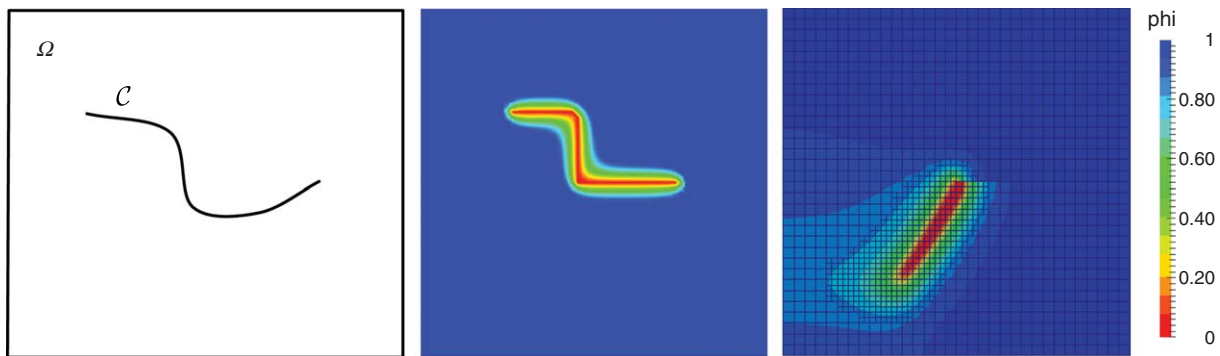


**Fig. 1**—A lower-dimensional crack  $C \in \mathbb{R}^{d-1}$  (left) and its diffuse approximation in  $\mathbb{R}^d$  (middle and right) inside a bounded reservoir domain  $\Omega \in \mathbb{R}^d$ . The crack is represented by red color, the diffusive transition zone  $\varepsilon$  by green color, and the unbroken material by blue color. In the right figure, the crack resolution is enhanced by using adaptive local grid refinement developed by Heister et al. (2015).

by a bandwidth  $2\varepsilon$  (see Fig. 1, the yellow/green zones), by a phase-field function  $\varphi$ . The phase-field function is an indicator function with values between zero and unity inside and outside of the crack, respectively. This diffusive or mushy zone also provides a smooth interpolation for an interface between a fracture and the reservoir. A coupling of reservoir fluids and geomechanics allows a comprehensive study of this multiscale problem in which only few results were published to date (e.g., Dean and Schmidt 2008 and Lujun et al. 2007). We also present an algorithm to integrate fracture growth with our reservoir simulator IPARS (implicit parallel accurate reservoir simulator). This allows for both short-term transient pressure analysis and long-term recovery predictions. Please note that the terms “crack growth” or “fracture propagation” are used interchangeably in the following, and imply both variation in fracture width (or aperture) and its length (or surface area).

The major advantages of using phase-field modeling for crack propagation are as follows:

- The fixed-grid topology avoids expensive remeshing for resolving the exact fracture location. The model can therefore be implemented easily to simulate both 2D and 3D crack propagation.
- Fracture nucleation, propagation, kinking its and curvilinear path are intrinsically determined. This avoids computational overheads associated with post-processing of quantities such as stress-intensity factors.
- We can easily handle large fracture networks because complex phenomena of joining and branching do not require keeping track of fracture interfaces.
- Modeling crack growth in heterogeneous media does not require special treatment. Additionally, the crack-opening displacement (fracture aperture) can be calculated with the phase-field function.

The diffusive transition zone tends to smear out the sharp crack surface, and the characteristic length-scale parameter  $\varepsilon$  must be chosen accordingly. Here, an adaptive local grid-refinement technique (Heister et al. 2015) can be used to increase crack-surface resolution while keeping the computational costs low. In addition, some of the challenges associated with a nonconvex functional inherent to the phase-field formulation were also addressed by Heister et al. (2015). An illustration of local grid refinement and high resolution of the fracture path is provided in Fig. 1 (right).

The primary focus of this work is on the following aspects:

- Investigating the applicability of the phase-field approach for crack propagation in heterogeneous (permeability and geomechanical parameters) porous media.
- Studying the effect of fracture spacing and stress shadows on simultaneous and sequential multistage fracturing scenarios.
- Developing a work flow to couple the phase-field models to our reservoir simulator IPARS to study the effect of production stimulation on long-term recovery predictions.

In the following sections, we model fracture propagation caused by slickwater injection only, and therefore the fluid viscos-

ity is assumed to be constant. We account for varying reservoir complexities such as natural fractures, faults, and barriers with a comprehensive fractured poroelastic reservoir flow model. This allows for a two-stage production optimization because of (1) a well-engineered hydraulic-fracturing scheme followed by (2) an optimal fractured-well placement, considering far-from-wellbore reservoir complexities.

The paper is organized as follows: We first provide the motivation for this work and reasons for our choice of using a phase-field approach for modeling hydraulic fracturing. The governing equations for the phase-field fracture propagation approach and the reservoir flow equations are described in the model-formulation section. This is followed by a discussion on the coupling algorithm between the fracture-propagation model and our reservoir simulator. In the final section, numerical tests are presented to demonstrate the capabilities of the fracture-propagation models and the coupling scheme.

## Model Formulation

We briefly discuss the assumptions of the classical brittle-fracture theory (Griffith 1921) used later in the model formulation. The theory postulates two physical phenomena: (1) linear elasticity and (2) fracture propagation, as energy-dissipation mechanisms, strictly separated by a threshold (critical energy-release rate) assuming a sharp transition between fractured and nonfractured media. The criterion for brittle-fracture propagation assumes:

1. The crack growth is irreversible.
2. The energy-release rate is bounded above by a critical energy-release rate.
3. The crack grows if, and only if, the energy-release rate is critical.

One of the seminal works in phase-field studies was presented by Francfort and Marigo (1998) in which Griffith's laws are described in a variational setting. In our work, we use this variational approach and develop models for fracture propagation in a poroelastic medium. To this end, we present two different modeling approaches:

1. Pressurized phase-field fracture-propagation model
2. Fluid-filled phase-field fracture-propagation model

The first approach relies on a given (or assumed) time-varying pressure distribution whereas the second approach solves a flow model to calculate a pressure field as the crack evolves. A force equilibrium is assumed between fracture fluid-pressure and reservoir stresses normal to the fracture surface for both models. We first define a two-field problem in two unknowns: (1) a vector-displacement field  $u$  and (2) a scalar phase-field variable ( $\varphi$ ), assuming a known pressure field and call it the pressurized fracture-propagation approach. In this, the elasticity and phase-field equations are first formulated as an energy-minimization problem. The related weak form is then obtained in terms of the Euler-Lagrange equations by differentiating this energy-minimization functional with respect to the unknown variables  $u$  and  $\varphi$ . This serves as a

natural setting for using a Galerkin finite-element method for spatial discretization. We then extend this to a fluid-filled modeling approach in which the pressure field is calculated by solving a flow problem. The mass-conservation equation and Darcy's law describing fluid flow are expressed as a pressure-diffraction equation (Mikelić et al. 2015a).

Let  $\Omega \in \mathbb{R}^d$ ,  $d = 2, 3$  be the reservoir domain, as shown in Fig. 1 (left), with a (lower-dimensional) fracture  $\mathcal{C} \in \mathbb{R}^{d-1}$ . Further, let the external boundary of  $\Omega$  be denoted by  $\partial\Omega$ . We assume homogeneous Dirichlet conditions for the displacements on  $\partial_D\Omega$  of  $\partial\Omega$ . On the remaining part  $\Gamma_N = \partial_N\Omega$ , Neumann conditions are defined. Furthermore, the crack domain is  $\mathcal{C}$ , assumed to be smooth with  $n$  being the unit exterior normal to  $\Omega$ . Let the fractured and unfractured states be strictly represented by values zero and unity, respectively. A smooth approximation of the crack is then given by the indicator function that varies from zero to unity in a continuous fashion. Fig. 1 (right) shows the  $d$ -dimensional approximation of a lower dimensional crack  $\mathcal{C}$  by use of a smooth indicator function defined on the reservoir domain  $\Omega$ . Here, the lowest and highest values are represented by red and blue color, respectively.

**Pressurized Fracture-Propagation Model.** Here, we present the pressurized fracture-propagation model as a two-field problem in two unknowns: displacement  $u$  and phase-field variable  $\varphi$ . A known spatial distribution of the pressure field is assumed which changes temporally. We also assume that the fracture is infinitely conductive. Hence, the pressure variation can be assumed to be negligible along the fracture length (or area). The pressure field in the reservoir domain  $\Omega$  is therefore chosen such that it is spatially invariant at the crack  $\mathcal{C}$ . Assuming an a priori pressure field  $p$ , the energy of a poroelastic medium  $\Omega$  with a crack  $\mathcal{C}$  is given by

$$E(u) = \underbrace{\frac{1}{2} \int_{\Omega} \sigma_E : e(u)}_{\text{Elastic energy}} - \underbrace{\int_{\Gamma_N \cup \mathcal{C}} \tau u}_{\text{Surface energy}} - \underbrace{\int_{\Omega} \alpha_B (p - p_0) \nabla \cdot u}_{\text{Pore-pressure contribution}}, \quad (1)$$

where the elastic stress tensor is denoted by  $\sigma_E := \mathcal{G}e(u)$ , where  $\mathcal{G} \in \mathbb{R}^4$  is the fourth-order Gassman tensor,  $e(u) = \frac{1}{2}(\nabla u + \nabla u^T)$  is the strain tensor,  $\alpha_B \in [0, 1]$  is the Biot's coefficient,  $p$  is the (given) pore pressure,  $p_0$  is the reference pressure,  $u$  is the displacement field, and  $\tau$  are the surface forces on the outer boundary  $\Gamma_N$  and the fracture  $\mathcal{C}$ . The linear stress/strain relationship is given by

$$\sigma_E = 2\mu e(u) + \lambda \text{tr}[e(u)]I, \quad (2)$$

$$e(u) = \frac{1}{2}(\nabla u + \nabla u^T), \quad (3)$$

where  $\text{tr}$  denotes the trace of a matrix; that is,  $\text{tr}(A) = A_{11} + A_{22} + A_{33}$ , where  $A_{ii}$ ,  $i = 1, 2, 3$  are the diagonal entries of  $A$ . Furthermore,  $\mu$  and  $\lambda$  denote the Lamé parameters, and please note that the energy functional represented by Eq. 1 only takes into account the red surface force (stress boundary condition) at the crack  $\mathcal{C}$ . Extending the energy functional given by (1) to include crack growth by accounting for the energy-release rate associated with an increase in fracture length (or surface area)  $\mathcal{C}$ , we obtain

$$E(u, \mathcal{C}) = \underbrace{\frac{1}{2} \int_{\Omega} \sigma_E : e(u)}_{\text{Elastic energy}} - \underbrace{\int_{\Gamma_N \cup \mathcal{C}} \tau u}_{\text{Surface energy}} - \underbrace{\int_{\Omega} \alpha_B (p - p_0) \nabla \cdot u}_{\text{Pore-pressure contribution}} + \underbrace{G_c \mathcal{H}^{d-1}(\mathcal{C})}_{\text{Fracture energy}}, \quad (4)$$

where  $G_c$  is the critical elastic energy-release rate depending on the material and is determined experimentally and  $\mathcal{H}^{d-1}$  is the length (2D) or surface area (3D) of the fracture. Here,  $G_c$  is

related to stress-intensity factor under assumptions on the material properties such as an isotropic, linear elastic solid (Irwin 1958). The interaction of fracture ( $p_F$ ) and reservoir ( $p_R$ ) pressures is modeled in terms of an interface law. We assume that the fracture length (or surface area) is much larger than its width (or aperture). Therefore, a lubrication approximation of the stress at the interface  $\mathcal{C}$  is a plausible choice. The fracture pressure  $p_F$  is in equilibrium with the normal component of reservoir stress at the crack  $\mathcal{C}$  such that

$$\sigma n = [\mathcal{G}e(u) - \alpha p_R I]n = -p_F n. \quad (5)$$

Here,  $\sigma$  is the total stress; namely,  $\sigma = \sigma_E - \alpha p_R I$  and  $n$  is the normal unit vector. Further assuming pressure continuity at  $\mathcal{C}$ , the pressure field  $p$  is such that  $p = p_F$  on  $\mathcal{C}$  and  $p = p_R$  in  $\Omega \setminus \mathcal{C}$ . The fracture-pressure contribution is reflected in the surface force integral, second term in the right-hand side of Eq. 4, over  $\mathcal{C}$  as

$$\begin{aligned} \int_{\mathcal{C}} \tau u &= \int_{\mathcal{C}} \sigma n u = - \int_{\mathcal{C}} p u n = - \int_{\Omega} \nabla \cdot (p u) + \int_{\Gamma_N} p u n \\ &= - \int_{\Omega} (u \cdot \nabla p + p \nabla \cdot u) + \int_{\Gamma_N} p u n, \end{aligned} \quad (6)$$

resulting in a volumetric representation for the pressure. We assume Dirichlet boundary conditions for pressure on  $\Gamma_N$ , and therefore, the last term in Eq. 6 vanishes. By substituting Eq. 6 in Eq. 4, one can write the energy functional as

$$E(u, \varphi) = \frac{1}{2} \int_{\Omega} \sigma_E : e(u) - \int_{\Gamma_N} \tau u - \int_{\Omega} (\alpha_B - 1) \nabla \cdot u + \int_{\Omega} u \cdot \nabla p + \int_{\Omega} \alpha_B p_0 \nabla \cdot u + G_c \mathcal{H}^{d-1}(\mathcal{C}). \quad (7)$$

Following the approach presented by Ambrosio and Tortorelli (1990, 1992), one can approximate the fracture length (or surface area) ( $\mathcal{H}^{d-1}$ ) in a 2D (or 3D) domain with an elliptic functional as

$$\mathcal{C}_\varepsilon = \frac{1}{2\varepsilon} \|1 - \varphi\|^2 + \frac{\varepsilon}{2} \|\nabla \varphi\|^2, \quad (8)$$

thereby, introducing a variable  $\varphi$ , referred to as the phase-field variable hereafter. The phase-field variable is defined as a continuous quantity on the entire domain  $\Omega$  for a time span varying from 0 to T. A careful examination of Eq. 8 shows, for a given value of  $\varepsilon > 0$ , this functional assumes lowest values when  $\varphi$  is a constant assuming values of either 0 (fracture) or 1 (porous-rock matrix). We notice that the phase-field approach is related to gradient-type material modeling with a characteristic length-scale. Here,  $\varepsilon$  is a regularization parameter and can be considered, as such, a length-scale parameter that has a physical meaning (Miehe et al. 2010; Pham et al. 2011). The second term ensures that  $\varphi$  changes smoothly between 0 and 1, allowing the representation of the fracture as a diffuse interface. Eq. 8 represents a mathematically consistent approximation of the true crack  $\mathcal{H}^{d-1}$ . The elastic and pore-pressure contributions in Eq. 4 are well defined for the porous-rock matrix excluding the crack ( $\Omega \setminus \mathcal{C}_\varepsilon$ ) and cease to exist in the crack  $\mathcal{C}_\varepsilon$ . This discontinuity is handled by regularization Eq. 9 that provides a smooth approximation to the poroelastic contributions over the entire domain  $\Omega$ . By defining  $\varphi$  over the entire domain, one can approximate the volume integrals correspondingly:

$$\frac{1}{2} \int_{\Omega} \sigma_E : e(u) \rightarrow \frac{1}{2} \int_{\Omega} [(1 - \kappa) \varphi_+^2 + \kappa] \sigma_E : e(u). \quad (9)$$

Here,  $\varphi_+$  is the maximum of  $\varphi$  and 0,  $\kappa \approx 0$  (determined by machine precision) is a positive regularization parameter for the elastic energy. Similarly, to satisfy Assumptions 2 and 3, the energy functional Eq. 4 is regularized with  $\varphi$  as follows:



$$E_\varepsilon(u, \varphi) = \frac{1}{2} \int_{\Omega} [(1 - \kappa)\varphi_+^2 + \kappa]\sigma_E : e(u) - \int_{\Gamma_n} \tau u \\ - \int_{\Omega} (\alpha_B - 1)p\varphi_+^2 \nabla \cdot u + \int_{\Omega} u \cdot \nabla p \varphi_+^2 \\ + \int_{\Omega} \alpha_B p_0 \varphi_+^2 \nabla \cdot u + G_c \left( \frac{1}{2\varepsilon} \|1 - \varphi\|^2 + \frac{\varepsilon}{2} \|\nabla \varphi\|^2 \right). \quad (10)$$

The length-scale parameter  $\varepsilon$  denotes the width of the transition zone (see Fig. 1 in which we move from red to blue) as  $\varphi$  varies from zero to unity representing the cracked and uncracked states, respectively. With  $\varphi$ , the spatially lower dimensional crack  $C \in \mathbb{R}^{d-1}$  is approximated as a volume (or surface)  $C_\varepsilon \in \mathbb{R}^d$  with same spatial dimensions as the 3D (or 2D) domain  $\Omega \in \mathbb{R}^d$ . One can see from Eq. 10 that, if  $\varphi$  is 0 (fracture), the first and second terms become zero, and the energy functional is dominated by the critical energy-release rate  $G_c$ . Similarly, when  $\varphi$  is 1, the third term becomes zero. An intermediate behavior can be seen for values between zero and unity. It is well known that  $E_\varepsilon(u, \varphi)$  is not convex simultaneously in  $u$  and  $\varphi$  because of the bulk term

$$\int_{\Omega} [(1 - \kappa)\varphi_+^2 + \kappa]\sigma_E : e(u).$$

In Heister et al. (2015), a robust and accurate procedure on the basis of a time extrapolation was proposed to convexify  $E_\varepsilon(u, \varphi)$ . By linear extrapolation using the two previous timestep solutions  $\varphi^{n-1}$  and  $\varphi^{n-2}$ , we build  $\varphi$  such that

$$\int_{\Omega} [(1 - \kappa)\tilde{\varphi}_+^2 + \kappa]\sigma_E : e(u).$$

Finally, we strongly impose the irreversibility constraint (Assumption 1) on  $\varphi$ ; that is,

$$\partial_t \varphi \leq 0, \quad (11)$$

which ensures that the state variables change in the direction of energy minimization or entropy maximization, in accord with the 2nd law of thermodynamics. Time-discretization with a backward difference scheme leads to

$$\partial_t \varphi \leq 0 \Rightarrow \varphi - \varphi^n \leq 0, \quad (12)$$

where  $\varphi^n$  denotes the phase-field solution at the previous timestep. This approximation is used to define a penalization strategy to impose this constraint. The final energy functional then reads:

$$E_\varepsilon(u, \varphi) = \frac{1}{2} \int_{\Omega} [(1 - \kappa)\varphi_+^2 + \kappa]\sigma_E : e(u) - \int_{\Gamma_n} \tau u \\ - \int_{\Omega} (\alpha_B - 1)p\varphi_+^2 \nabla \cdot u + \int_{\Omega} u \cdot \nabla p \varphi_+^2 \\ + \int_{\Omega} \alpha_B p_0 \varphi_+^2 \nabla \cdot u + G_c \left( \frac{1}{2\varepsilon} \|1 - \varphi\|^2 + \frac{\varepsilon}{2} \|\nabla \varphi\|^2 \right) \\ + I_{K(\varphi^{n-1})}(\varphi), \quad (13)$$

where the last term  $I_{K(\varphi^{n-1})}(\varphi^n)$  is a penalization term to impose the irreversibility constraint Eq. 11. A simple strategy (as used in Mikić et al. 2013, 2015b) is given by

$$I_{K(\varphi^{n-1})}(\varphi) = \gamma[(\varphi - \varphi^{n-1})^+]^2, \quad (14)$$

for  $\gamma \rightarrow \infty$ .

The objective is to find displacement ( $u$ ) and phase-field variable ( $\varphi$ ) fields that minimize the energy functional  $E_\varepsilon(u, \varphi)$ . The Euler-Lagrange equations in variational form are thus obtained from the energy functional by differentiating the energy functional with respect to  $u$  and  $\varphi$  and setting each one to zero because it is the first-order necessary condition. The problem statement then reads: Find  $u$  and  $\varphi$  such that

$$\int_{\Omega} [(1 - \kappa)\varphi_+^2 + \kappa]\mathcal{G}e(u) : e(w) - \int_{\Gamma_n} \tau w \\ - \int_{\Omega} (\alpha_B - 1)(\varphi_+^2 p \nabla \cdot w) + \int_{\Omega} \varphi_+^2 w \cdot \nabla p = 0, \quad \dots \dots (15)$$

for all admissible test functions  $w$ ; as well as

$$\int_{\Omega} (1 - \kappa)\varphi_+ \mathcal{G}e(u) : e(u)\psi - \int_{\Omega} 2(\alpha_B - 1)(\varphi_+ p \nabla \cdot u)\psi \\ + 2 \int_{\Omega} \varphi_+ u \cdot \nabla p \psi + G_c \left( - \int_{\Omega} \frac{1}{\varepsilon} (1 - \varphi)\psi + \int_{\Omega} \varepsilon \nabla \varphi \nabla \psi \right) \\ + \int_{\Omega} (\Xi + \gamma(\varphi - \varphi^{n-1}))^+ \psi = 0, \quad \dots \dots (16)$$

for all admissible test functions  $\Psi$ . Here,  $\Xi$  and  $\gamma$  are a penalization function and parameter, respectively, to enforce the irreversibility constraint of crack growth with the help of an augmented Lagrangian formulation (Wheeler et al. 2014). The coupled system is rather uncommon because a time derivative only appears as the irreversibility constraint but not in the main equations. We notice that time enters the problem statement through time-dependent nonhomogeneous boundary conditions in the form of Dirichlet or Neumann conditions. Alternatively, through time-dependent term in the right-hand side as surface forces—here, the right-hand side values are given in form of the pressure  $p := p(t, x)$ .

**Fluid-Filled Fracture-Propagation Model.** The pressurized fracture-propagation model relies on a given pressure distribution in the reservoir and fracture. In this section, we extend this approach to develop a fluid-filled fracture-propagation model in which the pressure distribution is calculated by solving a flow problem. We present a coupled flow model for the reservoir and fracture. This, in conjunction with the fracture-propagation model, described previously, results in a coupled problem in three unknowns: displacement  $u$ , phase-field variable  $\varphi$ , and fluid pressure  $p$ . A slightly compressible flow is assumed for both reservoir and fracture, and the fluid densities are given by

$$\rho_j = \rho_j^0 \exp \left[ c(p_j - p_j^0) \right], \quad \dots \dots (17)$$

where,  $\rho_j$  is the fluid density,  $p_j^0$  the reference pressure,  $\rho_j^0$  the reference density, and  $c$  the fluid compressibility. Here  $j = F, R$  denotes the fracture and reservoir domains, respectively.

**Reservoir Flow ( $\Omega \setminus C$ ).** The mass-conservation equation for the reservoir domain is given by

$$\partial_t(\rho_R \phi) + \nabla \cdot (\rho_R v_R) = q_R \quad \text{in } \Omega \setminus C, \quad \dots \dots (18)$$

where,  $\phi$  is the porosity,  $\rho_R$  the fluid density, and  $q_R$  the source/sink term in the reservoir. A Darcy law is assumed which relates fluid velocity to gradient in pressure as

$$v_R = -\frac{K_R}{\nu} (\nabla p_R - \rho_R g). \quad \dots \dots (19)$$

Here,  $K_R$  is the permeability tensor,  $\nu$  the fluid viscosity, and  $g$  the gravity. Following Chen et al. (1995) and Coussy (1995, 2004), one can express the reservoir fluid fraction as

$$\phi_R = \phi_R^0 + \frac{1}{M} (p_R - p_R^0) + \alpha (\nabla \cdot u - \varepsilon_v^0), \quad \dots \dots (20)$$

with porosity  $\phi_R^0$ , volumetric strain  $\varepsilon_v^0$  and, pressure  $p_R^0$  at the reference state. Further,  $0 \leq \alpha \leq 1$ , where  $\alpha \in [0, 1]$ , is Biot's coefficient, and  $M > 0$  is the Biot modulus. Please note that in the following we use  $\nabla \cdot u$  and  $\varepsilon_v$  interchangeably.

A pressure-specified Dirichlet boundary condition is assumed everywhere on the boundary  $\partial\Omega$  of the domain  $\Omega$  for the flow problem given by

$$p = p^D \text{ on } \partial\Omega. \quad \dots \dots (21)$$

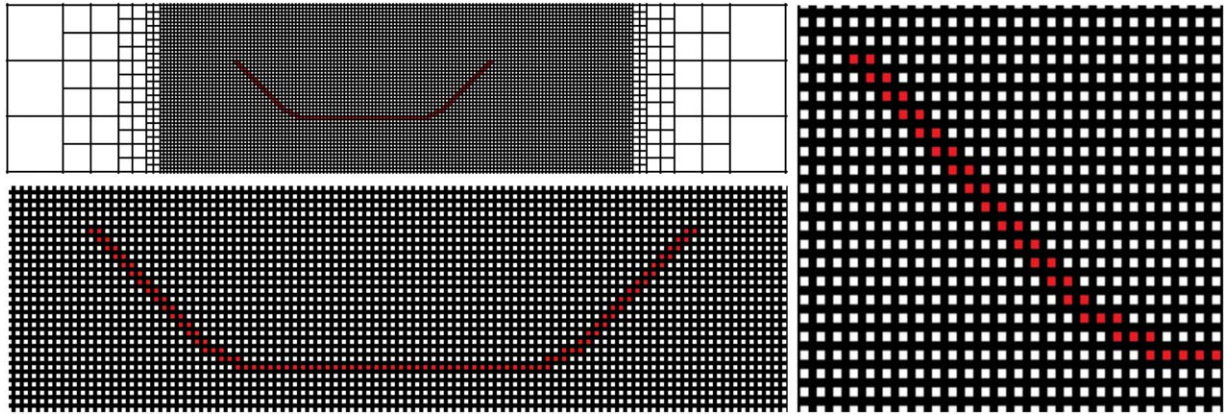


**Fig. 2—Determination of crack shape with a threshold for the phase-field variable to determine fracture cells (marked red).** Specifically, if for a point  $x := (x, y, z)$ ,  $\phi(x) < thr$ , then  $x \in \Omega_F$  (fracture); otherwise,  $x \in \Omega_R$  (reservoir). On the discrete level, this procedure is performed on a cellwise basis. Consequently, cells at location  $x$  with phase-field variable  $\phi(x) < thr$  are marked as fracture cells. The phase-field module uses locally refined grids with hanging nodes, which allows reducing the computational cost significantly. In this work, we refine a sufficiently large region around the fracture a priori while knowing how the fracture will grow: illustrated in the subfigure top left. An efficient and robust method in terms of “growing” meshes with predictor-corrector refinement was recently proposed by Heister et al. (2015); a result for illustration is provided in Fig. 1.

The fracture boundary  $\mathcal{C}$  is treated differently and is presented later in the pressure-diffraction formulation section. The fixed-stress iterative coupling scheme is then used to solve this coupled flow and mechanics problem. For a given fracture configuration (determined by the phase-field variable), we begin by iterating between the flow problem (for a given displacement) and the elasticity problem (for a given pressure field). After this system is converged, we solve for the phase-field variable  $\phi$ . For numerical stability (a contraction mapping in the case of nonfractured problems) of the fixed-stress iterative coupling scheme, a term is added to the flow equation [Gai 2004 (p. 57) or Kim et al. 2009; Mikelić et al. 2013] such that the reservoir porosity can be rewritten as

$$\phi_R = \phi_R^0 + \left( \frac{3\alpha^2}{3\lambda + 2\mu} + \frac{1}{M} \right) (p_R - p_R^0) + \frac{3\alpha}{3\lambda + 2\mu} (\bar{\sigma} - \bar{\sigma}^0), \quad (22)$$

where the mean stress is given by  $\bar{\sigma} = \frac{3\lambda + 2\mu}{3} \varepsilon_v - \alpha p_R$ . Also,  $\bar{\sigma}^0$  is the mean stress at the reference state, and  $\lambda$  and  $\mu$  are the Lamé parameters. Substituting Eq. 22 in Eq. 18, we obtain

$$\partial_t \rho_R \left[ \left( \frac{3\alpha^2}{3\lambda + 2\mu} + \frac{1}{M} \right) p_R + \frac{3\alpha}{3\lambda + 2\mu} \bar{\sigma} \right] + \nabla \cdot (\rho_R v_R) = q_R \quad \text{in } \Omega \setminus \mathcal{C}. \quad (23)$$

**Fracture Flow ( $\mathcal{C}$ ).** The mass-conservation equation for the fracture is given by

$$\partial_t \rho_F + \nabla \cdot (\rho_F v_F) = q_F - q_L \quad \text{on } \mathcal{C}, \quad (24)$$

where,  $q_L$  is the leakage term for flow between reservoir and fracture,  $q_F$  the source/sink term, and  $\rho_F$  and  $v_F$  are the fluid density and velocity in the fracture, respectively. The fracture porosity is set to one in Eq. 24, and the fracture volume is accounted for later by the spatial discretization. The leakoff term accounts for flow interactions between the fracture and its adjacent porous medium, and is calculated as

$$q_L = (v_R \cdot n)_{\mathcal{C}} = v_R \cdot n|_{\mathcal{C}^-} - v_R \cdot n|_{\mathcal{C}^+}. \quad (25)$$

Here,  $[v_R \cdot n]_{\mathcal{C}}$  is the jump of the reservoir fluxes across the crack  $\mathcal{C}$ . A special relation for  $q_L$  was derived in Mikelić et al. (2015a) as a result of interface conditions as opposed to the phenomenological Carter model (Carter 1957). The term  $q_F$  denotes fluid injection into the fracture, which is modeled by a Dirac delta function point injection (Kreyszig 2010). This is equivalent to a rate-specified

injection well commonly used for flow modeling in reservoir engineering (Peaceman 1978). Alternatively, one can also use a well model to determine injection rates for the fracture but is left out for the sake of simplicity. Further, the fluid velocity in the fracture ( $v_F$ ) is assumed to satisfy Reynold’s lubrication equation given by

$$v_F = -\frac{w(u)^2}{12\nu} (\nabla p_F - \rho_F g). \quad (26)$$

The lubrication equation is a plausible choice, assuming fracture permeabilities are much larger than reservoir ( $K_F \gg K_R$ ). A comparison of Darcy’s law and Reynold’s lubrication equation shows that  $K_F = \frac{w(u)^2}{12\nu}$ , where  $w(u)$  is the fracture width (or aperture). The width  $w(u)$  is calculated as jump in normal displacements, in the reservoir domain, across the fracture  $\mathcal{C}$ .

**Pressure-Diffraction Formulation.** We now develop a single pressure formulation for the entire domain  $\Omega \in \mathbb{R}^d$  including the fracture. This is achieved by approximating the flow problem for lower dimensional crack  $\mathcal{C} \in \mathbb{R}^{d-1}$  as  $\Omega_F \in \mathbb{R}^d$  with the phase-field function  $\phi$  explained later (Fig. 2). To this end, we introduce an indicator function  $\chi$  to distinguish between the reservoir ( $\Omega_R$ ) and fracture domains ( $\Omega_F$ ). We extend the previous equations on the whole domain  $\Omega = \Omega_F \cup \Omega_R$  by defining

$$\chi_R := \chi_{\Omega_R}(t) = 1 \quad \text{in } \Omega_F(t), \quad (27)$$

$$\chi_F := \chi_{\Omega_F}(t) = 0 \quad \text{in } \Omega_R(t), \quad (28)$$

such that  $\chi_{\Omega_F} = 1 - \chi_{\Omega_R}$ . A decomposition of the domain is achieved by using the phase-field variable  $\phi$  as indicator function. Let  $0 \leq thr \leq 1$  be a threshold; then,

$$\phi \leq thr \Rightarrow \chi_F = 1, \quad (29)$$

$$\phi > thr \Rightarrow \chi_F = 0. \quad (30)$$

For numerical treatment, we use the phase-field variable as the smoothed indicator function with a continuous transition between 0 and 1. A fully coupled (monolithic) fluid-flow system is then given by

$$\begin{aligned} & \chi_{\Omega_R} \left( \frac{3\alpha^2}{3\lambda + 2\mu} + \frac{1}{M} \right) \partial_t p_R + \chi_{\Omega_R} \nabla \cdot (\rho_R v_R) \\ & = \chi_{\Omega_R} q_R - \chi_{\Omega_R} \partial_t \left( \frac{3\alpha}{3\lambda + 2\mu} \bar{\sigma} \right) \quad \text{in } \Omega, \end{aligned} \quad (31)$$

$$\chi_{\Omega_F} c \partial_t p_F + \chi_{\Omega_F} \nabla \cdot (\rho_F v_F) = \chi_{\Omega_F} q_F \quad \text{in } \Omega. \quad (32)$$

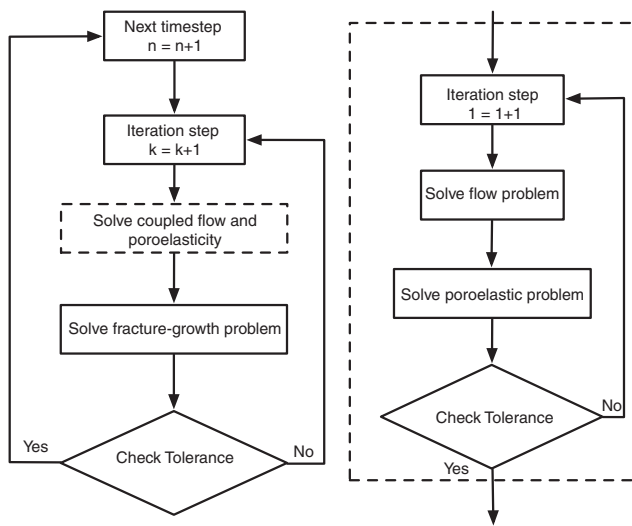


**Fig. 3—Flow chart for the augmented Lagrangian fixed-stress algorithm. The left and right flow charts show the augmented Lagrangian and fixed-stress algorithms, respectively.**

The resulting coupled system is of generalized parabolic type with discontinuous coefficients and is a diffraction problem (Ladyzhenskaja et al. 1968). The (generalized) pressure diffraction equation with Darcy's law Eq. 19 reads:

$$\theta \partial_t p - \nabla \cdot K_{eff} (\nabla p - \rho^0 g) = \tilde{q} \quad \text{in } \Omega, \quad (33)$$

where

$$\begin{aligned} \theta &:= \theta(x, t) := \chi_{\Omega_R} \theta_R + \chi_{\Omega_F} \theta_F \\ &= \chi_{\Omega_R} \left\{ \left[ \frac{3\alpha^2}{3\lambda + 2\mu} (\rho_R + c p_R + c \bar{\sigma}) + \frac{1}{M} (\rho_R + c p_R) \right] \right\} + \chi_{\Omega_F} c, \end{aligned} \quad (34)$$

$$\tilde{q} := \tilde{q}(x, t) := \chi_{\Omega_R} q_R - \chi_{\Omega_R} \partial_t \rho_R \left( \frac{3\alpha}{3\lambda + 2\mu} \bar{\sigma} \right) + \chi_{\Omega_F} q_F. \quad (35)$$

Here, the effective permeability  $K_{eff}$  is obtained by interpolation between the fracture permeability  $K_F$  and reservoir permeability  $K_R$  with the phase-field variable. For details, we refer to Mikelić et al. (2015a) and Remark 2.2 therein. Moreover, the gravity term  $g$  is rescaled and does implicitly contain the leakage term, as also discussed in Mikelić et al. (2015a), that is,  $g :=$

$\chi_{\Omega_R} g + \chi_{\Omega_F} \left( g + K_{eff}^{-1} \frac{v_{leak}}{\rho_F^0} \right)$ . The reservoir and fracture boundaries are now represented as  $\partial\Omega_R$  and  $\partial\Omega_F$  which intersect at  $\Gamma := \partial\Omega_F \cap \partial\Omega_R$ . In addition, two interface conditions must be satisfied at  $\Gamma$ , namely: the continuity of pressure  $p$  and continuity of normal fluxes  $v$ , and are given by

$$[p] = 0, \quad (36)$$

$$[K_{eff} \rho (\nabla p - \rho g)] \cdot n = 0, \quad (37)$$

where  $[a] := a|_{\Gamma^-} - a|_{\Gamma^+}$  denotes the jump in quantity  $a$ . Further, the flux continuity Eq. 37 interface condition accounts for the leakage term, given by Eq. 25.

## Numerical Discretization and Solution Algorithm

In this section, we present the discretization scheme for the three-field problem: pressure, elasticity, and phase-field. The pressurized fracture-propagation problem is a subset of the fluid-filled fracture-propagation problem whereby the pressure-field calculation is

neglected assuming pressures are known a priori. This is now easily achieved by using the fixed-stress iterative scheme: for a given fracture configuration (determined by the phase-field variable), we begin by iterating between the flow problem (displacements are known from the previous iteration) and the elasticity problem (the pressure field is known from the previous iteration). After this system is converged, we solve for the phase-field variable  $\phi$ . The coupling schemes are presented in Algorithm 1 and the flow chart in Fig. 3.

A backward Euler scheme is used for temporal discretization followed by spatial discretization with a conforming continuous Galerkin finite-element method on a hexahedral grid. The mesh size is characterized by parameter  $h$ . Here, all variables are discretized by continuous bilinears (or trilinears) in 2D (or 3D) space. The function spaces to realize a conforming finite-element method are denoted by  $U_h \subset U, V_h \subset V, W_h \subset W$ , where the index  $h$  denotes the spatial discretization parameter. We use the principle of virtual work to define variational (weak) formulations for the pressure (Eq. 38), linear elasticity (Eq. 39), and the nonlinear phase-field (Eq. 40) problems as follows: For all times  $t$ , solve for  $p_h \in U_h, u_h \in V_h, \phi_h \in W_h$  such that

$$\begin{aligned} A_0(p_h, \phi_h) &= \Delta t^{-1} \int_{\Omega} \theta (p_h - p_h^{n-1}) \phi_h dx \\ &+ \int_{\Omega} K_{eff} (\nabla p_h - \rho^0 g) \cdot \nabla \phi_h dx - \int_{\Omega} q \phi_h dx = 0 \quad \forall \phi \in U_h, \end{aligned} \quad (38)$$

and

$$\begin{aligned} A_1(u_h, w_h) &= \int_{\Omega} [(1 - \kappa) \phi_{h+}^2 + \kappa] \mathcal{G}e(u_h) : e(w_h) dx \\ &- \int_{\Gamma_N} \tau w_h ds - (\alpha - 1) \int_{\Omega} \phi_{h+}^2 p, \operatorname{div} w_h dx \\ &+ \int_{\Omega} \phi_{h+}^2 \nabla p_h w_h dx = 0 \quad \forall w_h \in V_h, \end{aligned} \quad (39)$$

and

$$\begin{aligned} A_2(\phi_h)(\psi_h) &= (1 - \kappa) \int_{\Omega} \phi_{h+} \mathcal{G}e(u_h) : e(u_h) \psi_h dx \\ &- 2(\alpha - 1) \int_{\Omega} \phi_{h+} p_h \operatorname{div} u_h \psi_h dx + 2 \int_{\Omega} \phi_{h+} \nabla p_h u_h \psi_h dx \\ &+ G_c \int_{\Omega} \left( -\frac{1}{\varepsilon} (1 - \phi_h) \psi_h + \varepsilon \nabla \phi_h \nabla \psi_h \right) \\ &+ \Delta t^{-1} \int_{\Omega} \left( \Xi + \gamma (\phi_h - \phi_h^{n-1}) \right)_+ \psi_h dx = 0 \quad \forall \psi_h \in W_h. \end{aligned} \quad (40)$$

Here,  $\gamma > 0$  denotes the augmented Lagrangian penalization parameter to treat the irreversibility constraint of crack growth and  $\Xi \in L^2(\Omega)$ . Moreover, the linear problem  $A_0$  is solved with a direct solver,  $A_1$  is solved with an iterative conjugate gradient solver and preconditioning, whereas the nonlinear problem  $A_2$  is solved with Newton's method (Wheeler et al. 2014) and herein the linear equations along with a direct solver. Eqs. 38 through 40 represent the discrete form of the fluid-filled fracture-propagation model equation. Here, we observe that, for a known (or given) pressure field  $p$ , there is no need to solve for Eq. 38. Thus, the discrete equations associated with pressurized fracture-propagation model are a subset of the fluid-filled fracture-propagation model.

The stability on the continuous level of the phase-field elasticity system for pressurized fractures was established in Mikelić et al. (2013, 2015b). Numerical simulations confirm the theory in these papers. Coupling the phase-field elasticity system for pressurized fractures with the pressure-diffraction equation by means of fixed stress (as performed in the current paper) was shown to be stable in simulation results by Mikelić et al. (2015a). Theoretical analysis and numerical analysis were not yet established—first steps of goal-oriented a-posteriori error estimation for phase-field fracture in geomechanics are discussed in Wick (2015). For the Biot system (without fractures), finite-element stability is known



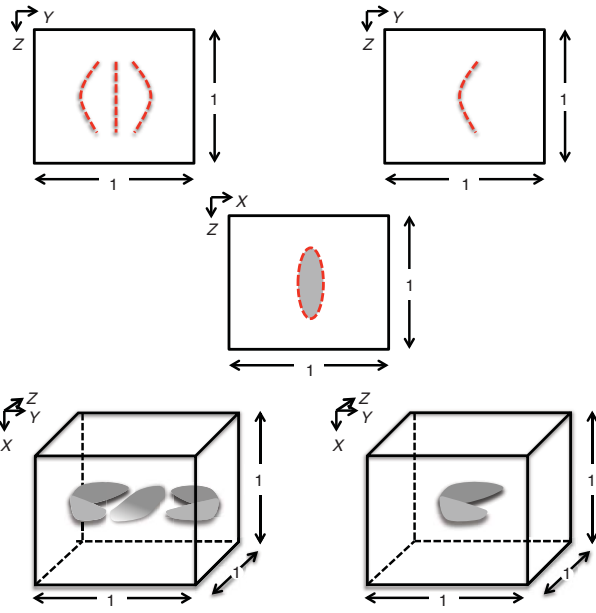


**Fig. 4—Work flow for reconstructing 3D fracture geometry from 2D information. A specific example used in the simulation is provided in Fig. 27. The spatial unit is m.**

(Liu 2004). Here, backward Euler and equal-order finite elements lead to a stable discretization. Likewise, finite elements of equal-order are known to work for phase-field fracture models (see Bourdin et al. 2000). By neglecting  $\Xi$  in Eq. 40, we arrive at a simple penalization scheme that is obtained by using Functional Eq. 14. Specifically,  $\gamma$  should be chosen in accordance with the discretization parameter  $h$ ; that is,  $\gamma \sim \frac{1}{h^2}$ . We note that  $h \ll \varepsilon$ , which requires fine meshes around the fracture(s). To this end, we use local mesh refinement with hanging nodes (see Fig. 2).

---

**Algorithm 1—Augmented Lagrangian Fixed-Stress Solution Algorithm:**

---

```

For each time  $t^n$ 
  repeat
    Solve augmented Lagrangian loop (outer loop)
    repeat
      Solve two-field fixed-stress (inner loop):
        Solve the pressure diffusion Eq. 38 with a Galerkin
        finite-element scheme
        Solve linear elasticity Eq. 39 with a Galerkin finite-
        element scheme
    until Stopping criterion

    
$$\max\{\|u_h^l - u_h^{l-1}\|, \|p_h^l - p_h^{l-1}\|\} \leq TOL_{FS}, \quad TOL_{FS} > 0$$


    for fixed-stress split is satisfied
      Solve the nonlinear phase-field in Eq. 40 with a Galerkin
      finite-element scheme
    Update

    
$$\Xi_{h,k+1} = (\Xi_{h,k} + \gamma(\varphi_{h,k+1} - \varphi_h^{n-1}))_+, \quad k = 0, 1, 2, \dots$$


  until Stopping criterion

  
$$\|\Xi_{h,k-1} - \Xi_{h,k}\| \leq TOL_{AL}, \quad TOL_{AL} > 0$$


  is satisfied
  Set:  $(u_h^n, \varphi_h^n) := (u_{h,k}, \varphi_{h,k})$ .
  Increment  $t^n \rightarrow t^{n+1}$ .
  
```

---

## Integrating Phase-Field Crack Propagation and Fractured-Reservoir Flow Models

In this section, we describe the proposed coupling method while outlining a workflow for translating fracture location, geometry, and width information between the phase-field crack-propagation model and the production-reservoir code. The use of hexahedral elements for spatial discretization in both models allows translation of fracture location and variables from one model to another. The phase-field with crack growth and localized flow is used as a preprocessor step for the fractured-reservoir flow. This results in a forward solution with the pertinent fracture geometry and width translated at the end of the propagation. We consider phase-field as an independent module that can be coupled to other codes. This assumes hydraulic-fracture growth to be a local or near-well-bore phenomenon that is not affected by far-field reservoir complexities such as reservoir boundaries, faults, and barriers. Under this assumption, the two processes hydraulic fracturing and later production are decoupled. Thus, a local flow problem with appropriate boundary conditions is solved to compute a local pressure-field during fracture propagation.

This forward coupling is computationally inexpensive, and adequately captures local flow-field variations affecting fracture growth. Another advantage is that the phase-field crack-propagation model generates fracture-growth information as a stand-alone module. The spatial and temporal scales associated with fracture growth and later production from a hydraulically fractured reservoir are widely different. Therefore, it is reasonable to treat the two processes separately. As discussed previously, the phase-field model includes a localized fluid-flow description and can therefore generate crack-growth information as a stand-alone. We then post-process and adapt this crack-geometry data for our fractured poroelastic reservoir simulator, resulting in a one-way coupling. This approach can be adapted for other legacy reservoir simulators.

**Projection of Variables/Mesh Reconstruction.** We start with the phase-field approach and solve for  $p$ ,  $u$  and  $\varphi$ . At the end of the fracturing process, the reservoir simulator needs the pressure  $p$  as initial pressure,  $\varphi$  to detect the shape of the fracture, and finally the width  $w := w(u)$ , which is computed as jump of the normal displacements. The shape of the fracture is determined for all  $\varphi < thr$ , where  $thr$  denotes a certain threshold, say  $thr = 0.1$  (see Fig. 2). If  $\varphi < thr$  in a cell, it is marked as fracture cell. All unknown quantities are computed at cell centers with the associated co-ordinate information to the reservoir simulator.

The fracture-growth calculations are computationally expensive for a 3D domain compared with 2D calculations. In this section, we present an alternative method to reconstruct 3D fracture geometry from two, 2D fracture-growth calculations in two orthogonal directions. Consequently, we propose a geometric multi-scale approach in which we only compute the cheaper 2D solution and reconstruct geometrically the corresponding 3D crack pattern by assuming symmetry in the third direction. Similar assumptions regarding symmetry were often used to construct analytical or semi-analytical solutions (Sneddon and Lowengrub 1969; Zhang et al. 2002). Fig. 4 outlines the schematic for such an approach. The fracture-propagation models, presented previously, are used to generate fracture patterns in a 2D domain for YZ and XZ planes. The rock-property information is kept the same for both the cases with an appropriate choice of boundary conditions in each plane. These are then combined to generate a 3D pattern at the end of crack growth.

The phase-field fracture-growth models, as described previously, use a fine-scale mesh for spatial discretization. However, for computational efficiency of long-term flow simulations, a coarse mesh is required. We therefore post-process and adapt this 3D fracture geometry, either obtained directly from the 3D crack-growth model or from the reconstruction procedure suggested previously, for use in a fractured poroelastic reservoir simulator. Fig. 5 shows an adaptation of the fracture geometry obtained from the crack-growth model in which a coarse mesh is used.

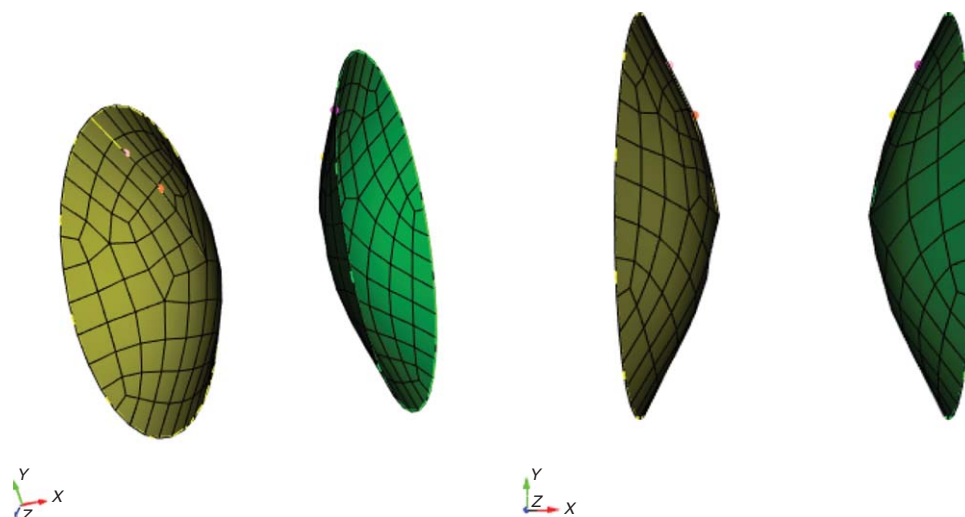


Fig. 5—Coarse fracture mesh after adaptation.

**Fractured-Well Model.** As previously described, the crack-propagation model already couples fracture flow to reservoir and is therefore complete in itself. That means, starting with a given setting, we start with that model and compute a fracture geometry, which might include curvilinear growth, branching, and joining. The fracture geometry is passed to the reservoir simulator, as described in the previous section. The width and the pressure information from the phase-field model are set as the initial conditions for the reservoir simulator. Fig. 6 (right) shows fractured-well placement (red blocks) in a reservoir with natural fractures (shaded orange). The mesh adaption is convenient because both models use hexahedral meshes, thus avoiding computationally costly interpolation between meshes with different mesh elements (such as tetrahedral and prisms).

The key advantage of our suggested ideas is concerned with the effort in coupling. Rather than iterating in each timestep between both frameworks, the phase-field is used as a preprocessor step and, as such, acts as an own module. This allows us to run different well-placement scenarios with the reservoir simulator with the same fracture geometry, avoiding redundant fracture-growth calculations for each scenario. The accuracy of the phase-field approach for modeling fracture propagation increases, as the mesh is refined. The spatial and temporal scales associated with crack propagation are much smaller compared with reservoir flow. Therefore, the use of a fine mesh for fracture-growth computations followed by reservoir-flow calculations on a coarse mesh is computationally efficient. To expedite the calculations for the phase-field fracture-growth model, we use a dynamic mesh-refine-

ment approach with locally refined grids and hanging nodes (see Fig. 2). For example, if we run 20 timesteps, we perform the first 15 on a coarse mesh, and refine the last 5 timesteps to get more accurate fracture tip and associated variable information. This procedure keeps the computational cost very reasonable.

## Numerical Tests

In this section, we present several numerical experiments in two and three dimensions to demonstrate model capabilities. The first set of results present simultaneous or sequential propagation of multiple fracture. Here, the effects of stress-shadowing and porous media heterogeneities on fracture path and growth rate are discussed. For the second set of results, we extract a fracture geometry from one of the fracture-growth scenarios and embed them in a coupled flow and mechanics reservoir simulator for long-term production evaluation. In the following, we provide geometry information and parameters for the test cases. Please note that the numerical results presented for fracture growth adhere to the SI unit system.

**Geometry, Grid, and Timestep Size Information.** The computational domain for all 2D tests is  $4\text{ m} \times 4\text{ m}$ . For the first test, an initial fracture length of 1 m is taken with midpoints at (1.5,2.0) and (2.5,2.0) for the two fractures. In the second test, the distance between the fractures is increased from 1 m to 2 m. For three fracture cases, we consider the midpoints (1,2), (2,2), and (3,2). Here, in the first test, all three fractures have the same length of 1 m, in

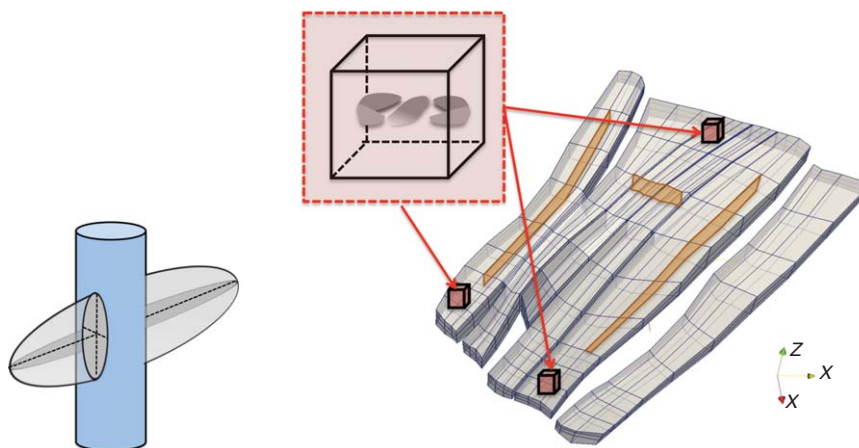


Fig. 6—Integrating fractures generated by phase-field model as a fractured-well model.



Penalization parameter ( $\gamma$ )	$10^4(2D)-10^3(3D)$
Regularization parameter ( $\kappa$ )	$10^{-6} \times h$
Regularization parameter ( $\varepsilon = 2h$ )	$0.088(2D)-1.09(3D)$
Fracture-injection rate ( $q_F$ )	$1 \text{ kg/m}^3$
Reservoir permeability ( $K_R$ )	$10^{-12} \text{ m}^2$
Biot parameter ( $M$ )	$2.5 \times 10^8 \text{ Pa}$
Biot coefficient ( $\alpha$ )	0 (decoupled)–1 (coupled)
Fluid compressibility ( $c$ )	$10^{-8} \text{ Pa}^{-1}$
Fluid viscosity ( $\nu$ )	$10^{-3} \text{ Pa.s}$
Reference density ( $\rho_0$ )	$1 \text{ kg/m}^3$
1st Lamé parameter ( $\mu$ )	$4.2 \times 10^7 \text{ Pa}$
2nd Lamé parameter ( $\lambda$ )	$2.8 \times 10^7 \text{ Pa}$
Fracture toughness ( $G_c$ )	$1.0 \text{ Pa.m}^{\frac{1}{2}}$

Table 1—Model parameters for phase-field, flow, and elasticity problems.

the second test the middle fracture has length 0.5 m, whereas in the final test, the middle fracture length is 1.5 m. For the 3D domain, a  $10 \text{ m} \times 10 \text{ m} \times 10 \text{ m}$  cube is taken with two two penny-shaped cracks with initial radius  $r=1.0 \text{ m}$  in the  $y=5.0$  plane with midpoints at  $(5.0, 3.0, 5.0)$  and  $(5.0, 7.0, 5.0)$ . The crack is approximated as a volume by extending it with the spatial-discretization parameter  $h$  in upward and downward (along  $y$ -axis) direction, respectively. As boundary conditions, we set the displacements zero on  $\partial\Omega$ . For each computation, we take 50 time-steps with timestep sizes of  $\Delta t=0.01$  seconds and  $\Delta t=0.005$  seconds for 2D and 3D domains, respectively.

**Model Parameters.** In all the examples next in the text, gravity  $g$  is assumed to be zero and the fluid is only driven by the point-source injection  $q$ . We perform computations with both  $\alpha=0$  and

$\alpha=1$  for decoupled and coupled flow and mechanics. However, it is important to note that  $\alpha=0$  and  $\alpha=1$  yield the same crack patterns if the characteristic time scale of the fracture is taken into account, as shown in Mikelić et al. (2015a). The characteristic fracture time scale is given by (using the Terzaghi's time scale as used similarly in Mikelić et al. 2015a),  $T_F = \frac{L^2 \eta_F c_F}{K_F} = \frac{1 \times 10^{-3} \times 10^{-8}}{10^{-8}} = 10^{-3}$ , in which we assumed a characteristic fracture length 1 m and characteristic fracture permeability  $K_F = 10^{-4} \text{ m}^2$ . Table 1 provides the model parameters where  $h$  is the size of square grid element.

### Fracture Propagation With Pressurized and Fluid-Filled Approaches.

Here, we present a numerical experiment to compare pressurized and fluid-filled fracture-propagation approaches presented previously. The elasticity and phase-field parameters are kept the same for the two cases. For the pressurized approach, a spatially invariant fracture pressure of  $2 \times 10^4 \text{ Pa}$  is assumed with increments by  $1 \times 10^4 \text{ Pa}$  with each timestep. The fluid-filled approach solves a coupled flow problem to obtain reservoir and fracture pressures with the flow parameters described previously. Figs. 7 and 8 show the crack evolution in time for the fluid-filled and pressurized fracture-propagation approaches, respectively. Here, fracture-growth rates and paths for the two approaches differ caused by differences in crack-pressure evolution. The fluid-filled approach is physically consistent because we solve a flow problem to calculate the fracture pressure. The pressure-field evolution for the fluid-filled approach is shown in Fig. 9.

**Fracture Propagation in 3D and 2D Domains.** In this example, we first show a numerical experiment simulating simultaneous propagation of two penny-shaped fractures in a 3D domain. This

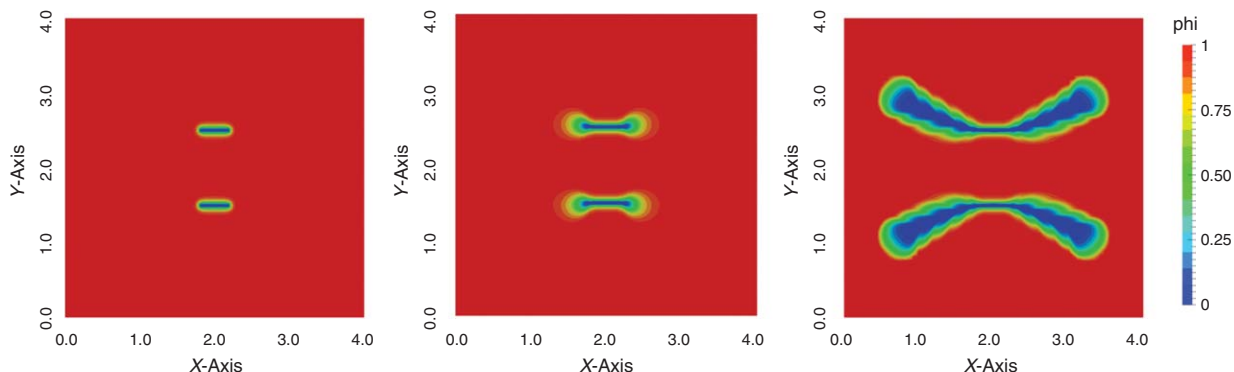


Fig. 7—Crack pattern for simultaneous propagation of two fractures with pressurized approach at  $T=0$  timesteps, 20 timesteps, and 30 timesteps in a 2D domain, which dimensions are in meters. The phase-field variable is dimensionless.

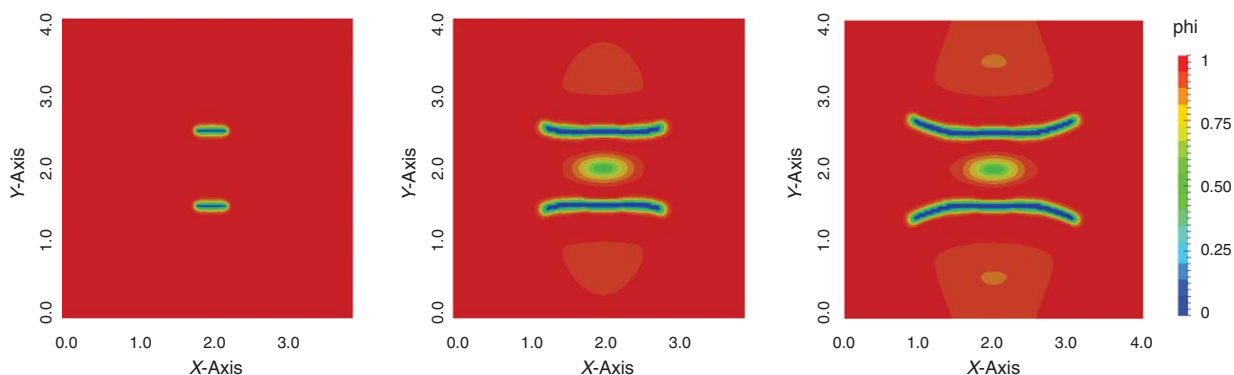
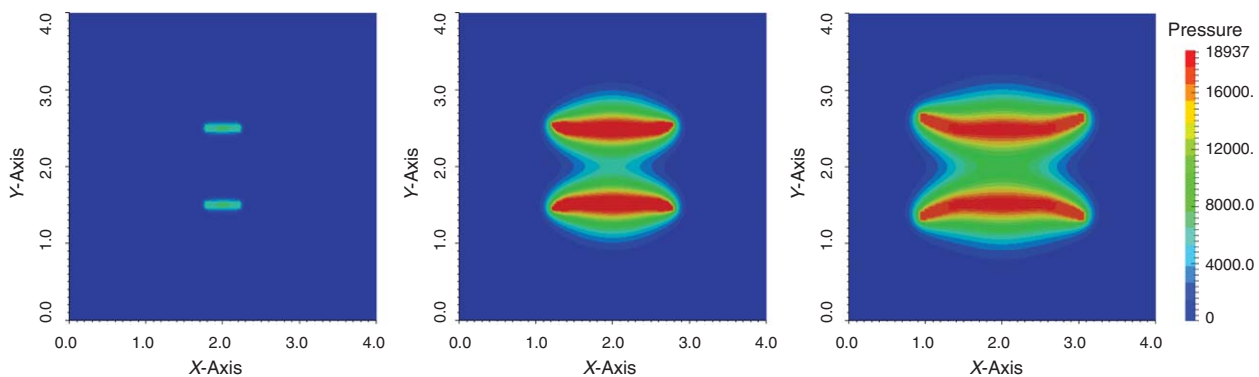
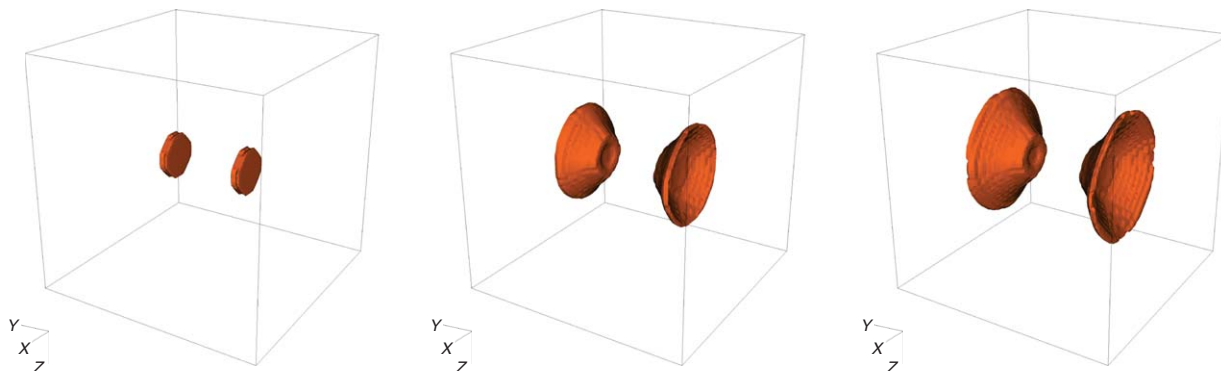


Fig. 8—Crack pattern for simultaneous propagation of two fractures with fluid-filled approach at  $T=0$  timesteps, 20 timesteps, and 30 timesteps in a 2D domain, which dimensions are in meters. The phase-field variable is dimensionless.



**Fig. 9—Pressure profile for simultaneous propagation of two fractures with fluid-filled approach at  $T=0$  timesteps, 20 timesteps and 30 timesteps in a 2D domain, which dimensions are in meters. The phase-field variable is dimensionless.**



**Fig. 10—Crack pattern for simultaneous propagation of two penny-shaped fractures at  $T=0$  timesteps, 15 timesteps, and 25 timesteps in 3D domain, which dimensions are in meters. The crack patterns are denoted in orange color.**

is followed by a 2D experiment, in a similar setting, to compare 2D and 3D results. **Fig. 10** shows fracture patterns during growth at  $T=0$ , 15 and 25 timesteps for the 3D case. Similarly, **Fig. 11** shows fracture locations at  $T=0$ , 20, and 30 timesteps for the 2D case.

**Fig. 12** shows that a high-stress magnitude between the two fractures at  $T=0$  and 20 timesteps results in diverging growth pattern. The phase-field models, presented here, account for external boundary conditions as well. The fracture-growth rate and path are therefore intrinsically determined by both near and far-field stresses depending on the vicinity of the fracture and the dominating effect. The stress distribution at  $T=30$  timesteps (**Fig. 12**) shows the effect of left and right boundaries.

Because the two cases presented here are symmetrical, the temporal variation of pressures at the centers of the two fractures, for each case, is similar. **Fig. 13** shows the time evolution of pressure at the center of one of the fractures for the 3D (left) and 2D

(right) domains. Note that the pressure builds up to threshold value and then starts dropping as the fracture starts growing. The results show resemblance of the fracture growth and transient pressure for the 3D and 2D cases. The 3D fracture geometry at the end of fracture growth will be used later for coupling with a fracture-reservoir flow simulator.

**Effect of Fracture Spacing on Fracture Growth.** In this section, we present a numerical experiment, similar to the 2D case presented earlier, with a larger initial fracture spacing and studying the resulting effect on the fracture pattern. The fracture locations at time  $T=0$ , 20, and 20 timesteps are shown in **Fig. 14**. One can observe by comparing **Figs. 13** and **14** that, as the spacing is reduced, the fracture pattern becomes diverging. This result demonstrates that an optimal fracture spacing can be achieved which maximizes reservoir-fracture interface area and therefore productivity.

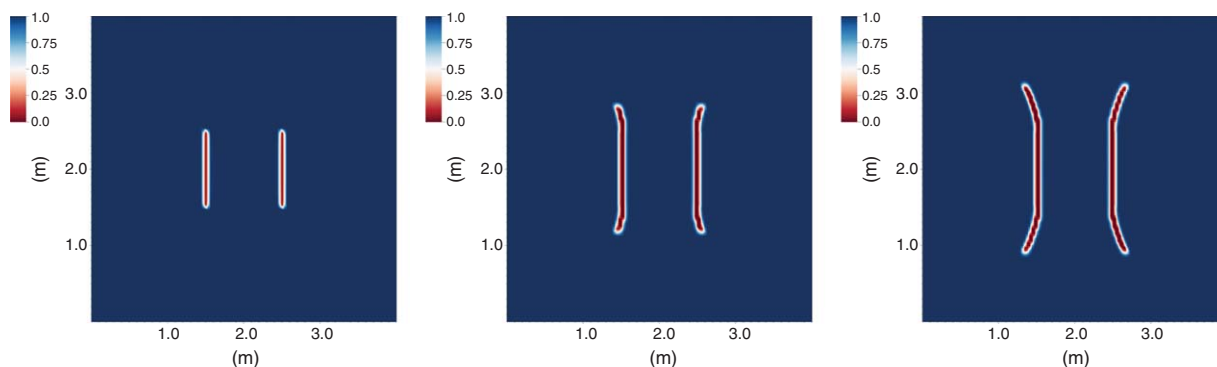


**Fig. 11—Crack pattern (displayed by the use of the dimensionless phase-field variable) for simultaneous propagation of two fractures at  $T=10$  timesteps, 25 timesteps, and 35 timesteps in a 2D domain.**

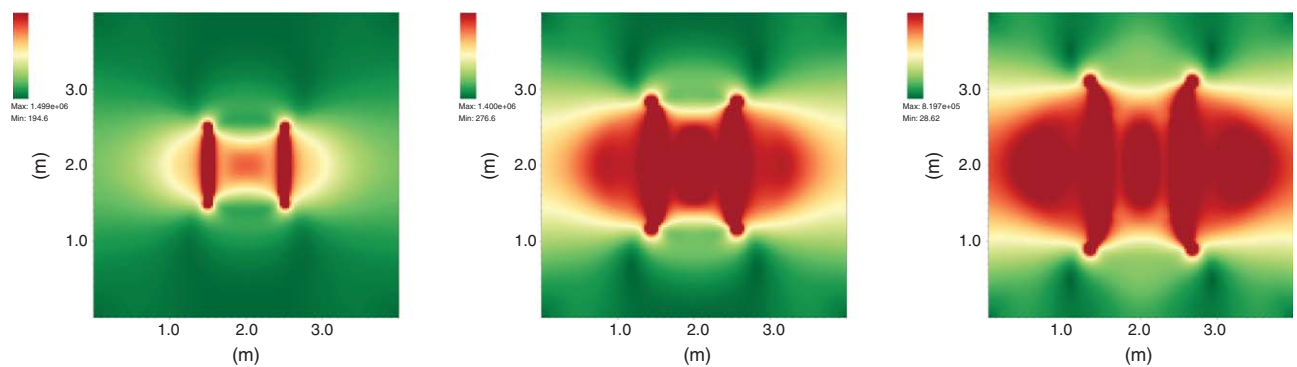


**Fig. 12—Stress distribution (with the SI unit Pa) for simultaneous propagation of two fractures at  $T=10$  timesteps, 25 timesteps, and 35 timesteps in a 2D domain.**

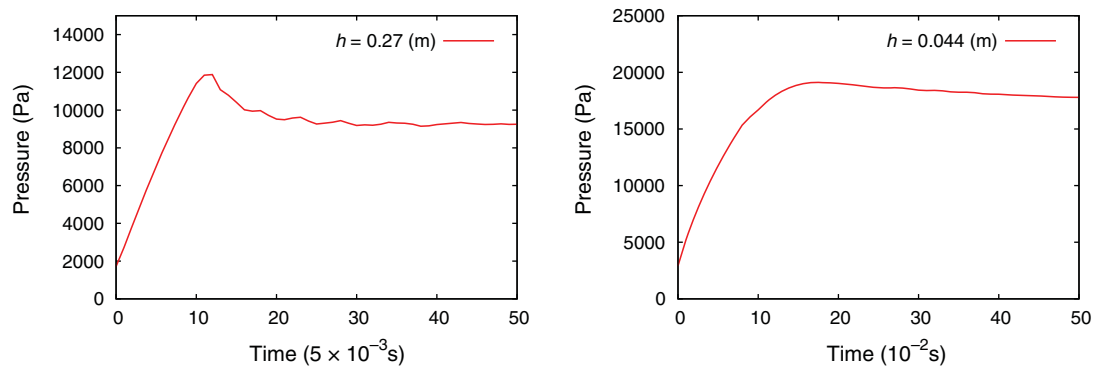


**Fig. 13—Transient pressure at the center of the fractures for 3D (left) and 2D (right) cases.**

**Fig. 15** shows that the stress magnitudes, at  $T=0$  and 20 timesteps, are higher toward the external boundaries and lower between the two fractures. Therefore, the fracture-growth pattern does not diverge, as in the previous case. A comparison between Figs. 12 and 15 clearly shows the differences.

**Effect of Discrete Fractures on Fracture Growth.** In this example, we study the effect of an existing fracture on the propagation of another fracture. This setting is devised to provide insight into growth patterns for sequential hydraulic fracturing. In **Fig. 16**, the left fracture is stationary, whereas the right fracture grows because of injection of hydraulic fluids. The stationary fracture (left) is given a higher material-stiffness property, compared with the reservoir, to replicate a propped fracture. As one can see, the hydraulic fracture does not show considerable pattern change because of the presence of an adjacent discrete fracture. Although a more-detailed study can be conducted to evaluate the combined effect of orientation, we restrict ourselves to the case of

parallel fracture for the sake of brevity. **Fig. 17** shows the stress fields (Frobenius norm) at times  $T=0$ , 20, and 40 timesteps. At timestep  $T=40$ , the fracture starts curving inward as the fracture tip approaches the external boundary where the boundary effect starts dominating.

**Effect of Heterogeneity on Fracture Growth.** In this set of tests, we extend the case of two simultaneous fracture propagations in a 2D domain to a heterogeneous porous media later in **Fig. 19** and nonconstant reservoir permeabilities later in **Fig. 20**. Randomly varying Lamé parameter fields are used with  $\mu = 4.2 \times 10^6 - 9.4 \times 10^7$  Pa and  $\lambda = 2.6 \times 10^6 - 9.3 \times 10^7$  Pa. Furthermore, a random distribution of permeability field is used with values varying between  $5 \times 10^{-12}$  m<sup>2</sup> and  $10^{-13}$  m<sup>2</sup>. In **Fig. 18**, the initial fracture locations and the material and permeability distributions are provided. We expect nonplanar fracture growth caused by spatially varying material properties. As before, we define two initial parallel fractures that grow as fluid is injected

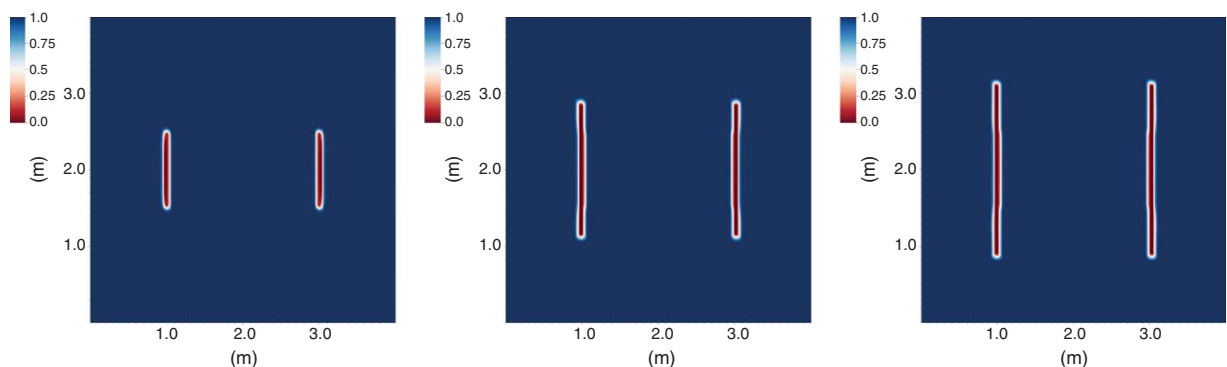


**Fig. 14—Crack pattern (with the dimensionless phase-field variable) for simultaneous propagation of two fractures, with larger spacing, at  $T=10$  timesteps, 25 timesteps, and 35 timesteps.**



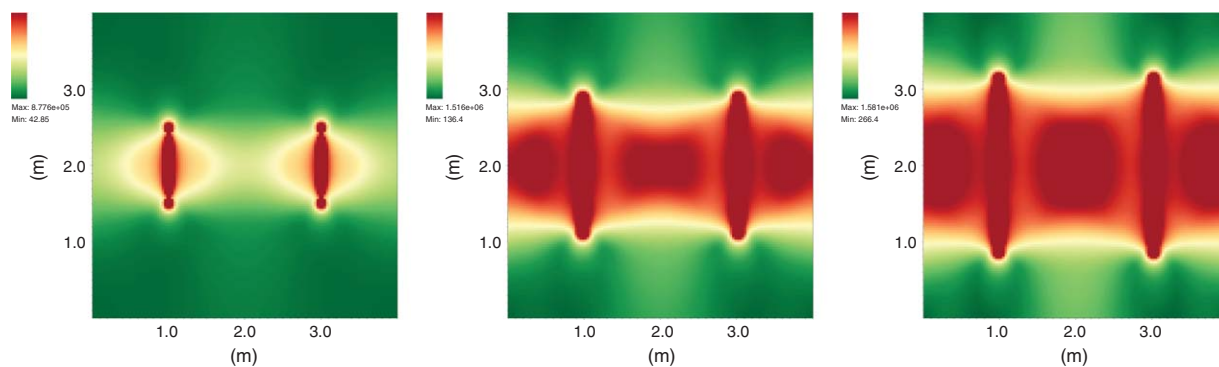


**Fig. 15—Stress distribution (displayed in the SI unit Pa) for simultaneous propagation of two fractures, with larger spacing, at  $T=0$  timesteps, 20 timesteps, and 30 timesteps.**

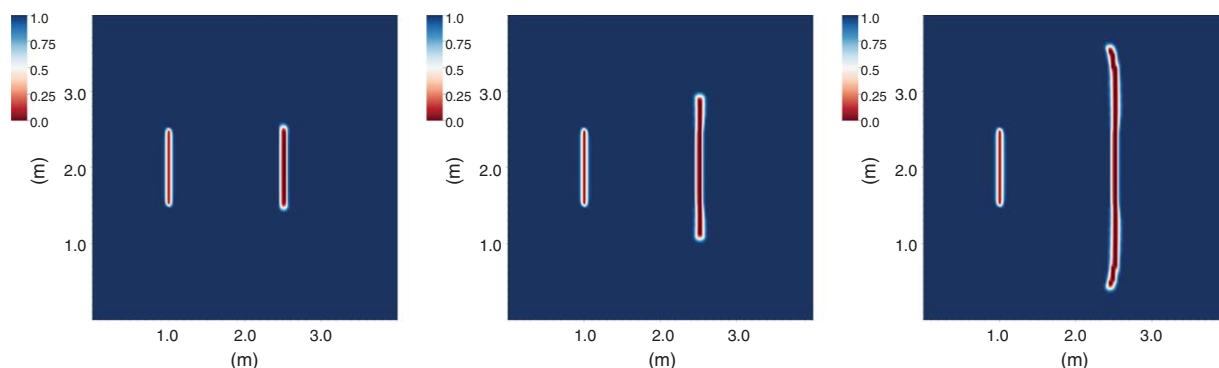


**Fig. 16—Crack pattern (displayed with the dimensionless phase-field variable) in the presence of a parallel discrete fracture at  $T=10$  timesteps, 20 timesteps, and 40 timesteps.**

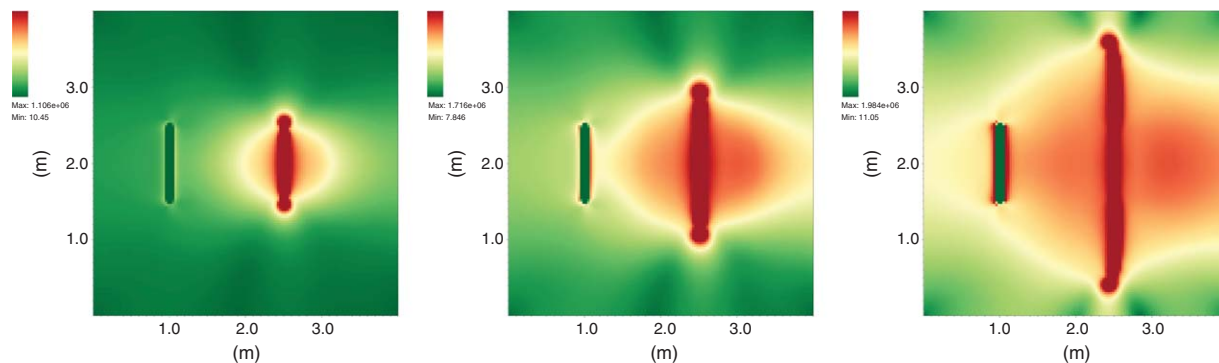


**Fig. 17—Stress-field variation (with the SI unit Pa) with crack growth in the presence of a parallel discrete fracture at  $T=0$  timesteps, 20 timesteps, and 40 timesteps.**

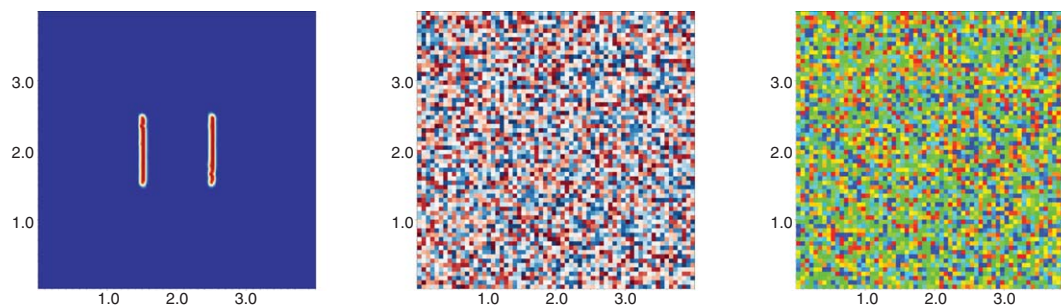


**Fig. 18—Initial crack pattern (left) with the dimensionless phase-field variable, randomly distributed Lamé coefficients (middle), and nonconstant permeability (right). The red denotes high values and blue/green denotes low values for the middle and right figures. All spatial dimensions are in meters.**

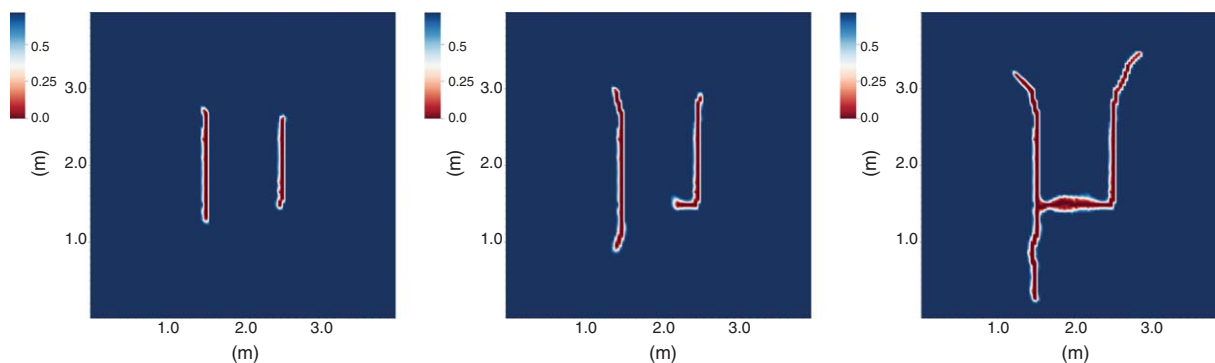


**Fig. 19—Crack pattern (with the dimensionless phase-field variable) for fracture propagation in a heterogeneous medium (Lamé coefficients) at  $T=20$  timesteps, 30 timesteps, and 50 timesteps.**

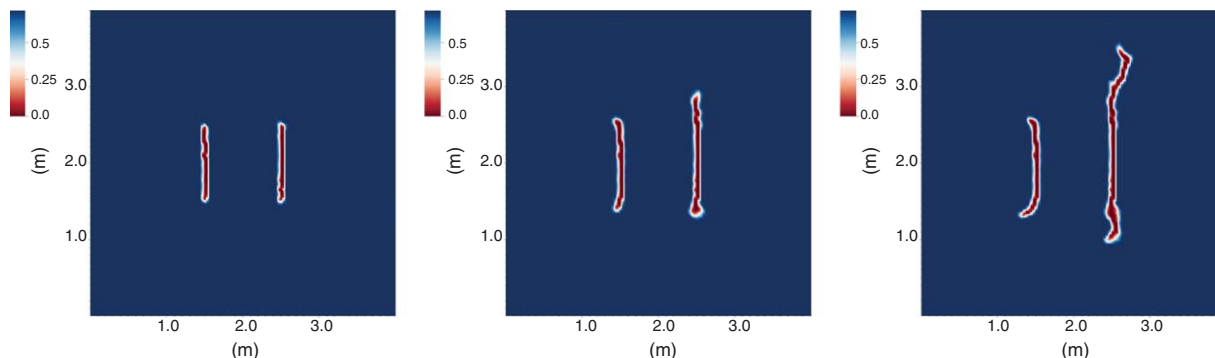


**Fig. 20—Crack pattern for fracture propagation in a heterogeneous medium (Lamé coefficients and permeabilities) at  $T=5$ , 10, and 15 timesteps.**

into each one of them. In **Fig. 19**, the right fracture joins the left fracture at  $T=50$  seconds. In the next simulation (**Fig. 20**), in addition to heterogeneous elastic media, a heterogeneous permeability field is assumed. We again observe a nonplanar crack growth including branching of the right fracture. Here, the two fractures do not join because the permeability heterogeneity prevents this phenomena compared with the case in which only heterogeneous Lamé parameters were used.

**Effect of Stress Shadowing on Fracture Growth.** Here, we investigate the effect of stress-shadowing and initial fracture nucleation lengths on fracture growth for simultaneous propagation of three fractures. The material properties (Lamé parameters) are kept homogeneous to accentuate observations and are by no means restrictive. Three cases were considered: (a) equal fracture nucleation lengths (**Fig. 21**), (b) shorter nucleation length for middle fracture (**Fig. 22**), and (c) longer nucleation length for middle fracture (**Fig. 23**). Please note that although boundary conditions play an important role in fracture growth, the emphasis here is solely on fracture/fracture interaction.

**Figs. 24, 25 and 26** show the stress fields (Frobenius norm) for the aforementioned three cases. In, **Fig. 21**, we observe that the growth of the middle fracture is shunned because of the stress-shadowing from the outer two fractures. Similar behavior is observed for the case with shorter nucleation length for middle fracture. However, the case with longer nucleation length for middle fracture shows contrasting behavior. Here, the stress shadow because of the middle fracture shuns the growth of outer fractures. This numerical test shows that a careful evaluation of stress-shadow effects is pivotal for planning a hydraulic-fracturing job, beginning from perforation to propagation with slick-water injection.

**Coupling the Phase-Field Model to a Reservoir Simulator.** In this section, we present an example to demonstrate the aforementioned approach for an explicit coupling of fracture growth to a reservoir simulator that is based on general hexahedral discretization (**Fig. 27**). A synthetic case is generated from Brugge-field geometry (e.g., Peters et al. 2009; Chen et al. 2010) in which the wells are augmented with hydraulic fractures. Here, the use of

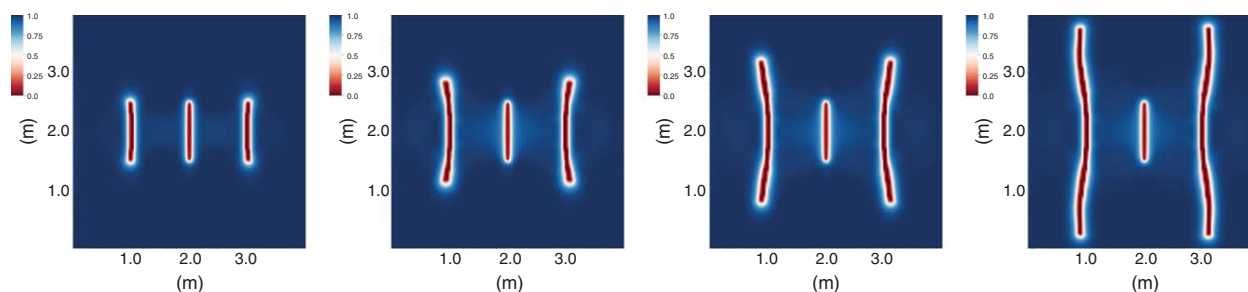


**Fig. 21—Crack pattern (with the dimensionless phase-field variable) at  $T=10$  timesteps, 20 timesteps, 30 timesteps, and 50 timesteps for three equidistant fractures, with equal initial fracture lengths.**

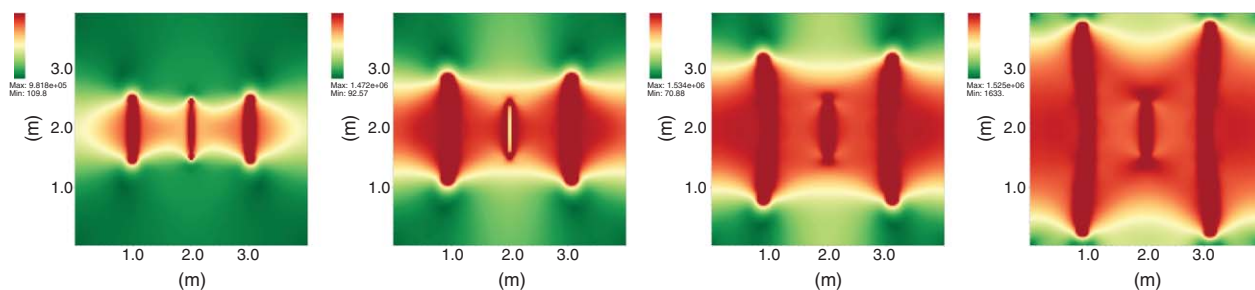


**Fig. 22—Crack pattern (with the dimensionless phase-field variable) at  $T=0$  timesteps, 20 timesteps, 30 timesteps, and 50 timesteps for three equidistant fractures, with smaller initial middle-fracture length.**

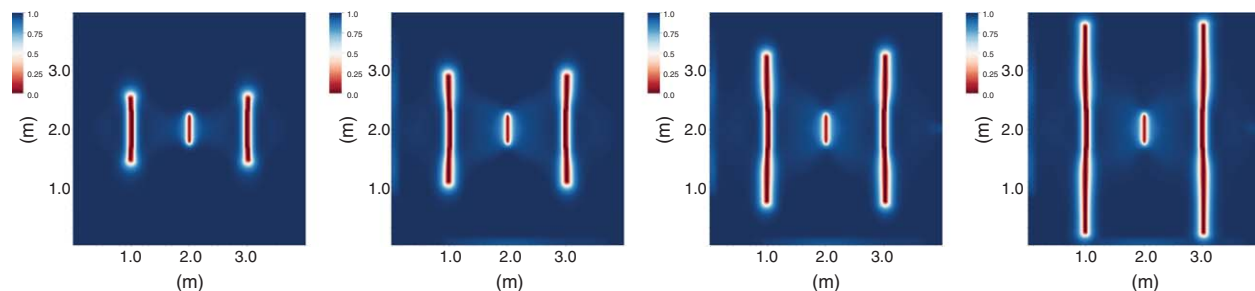


**Fig. 23—Crack pattern (with the dimensionless phase-field variable) at  $T=5$  timesteps, 10 timesteps, 20 timesteps, and 30 timesteps for three equidistant fractures, with longer initial middle-fracture length. The crack branching at  $T=30$  timesteps is caused by the boundary conditions.**

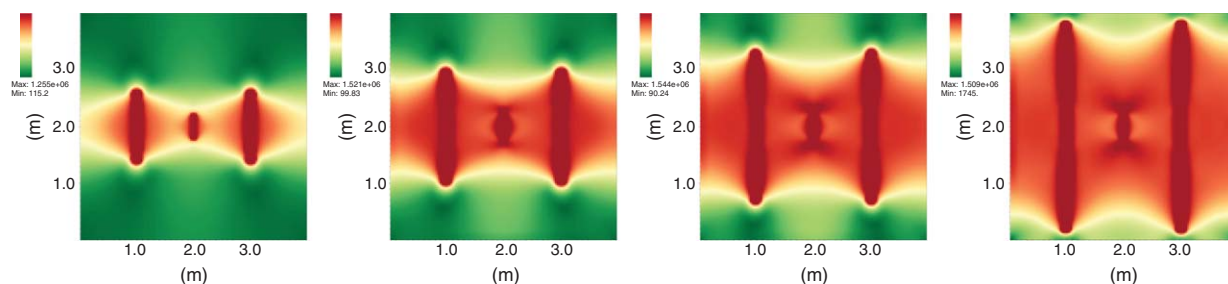


**Fig. 24—Stress-field variation (displayed in the SI unit Pa) with crack growth at  $T=10$  timesteps, 20 timesteps, 30 timesteps, and 50 timesteps for three equidistant fractures, with equal initial fracture lengths.**

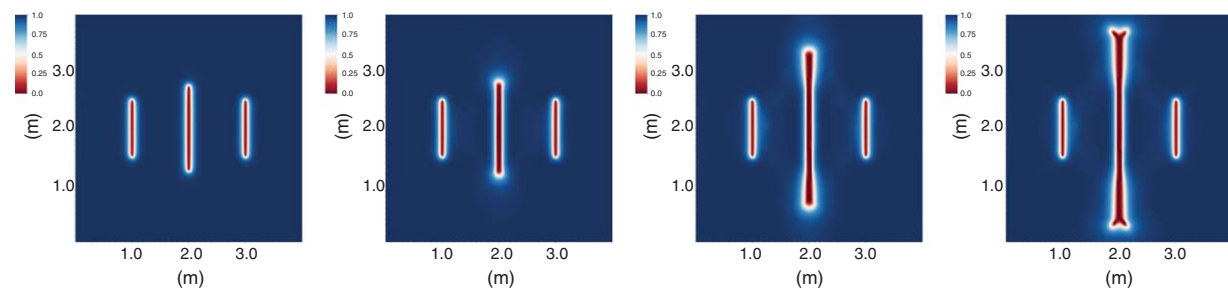


**Fig. 25—Stress-field variation (displayed in the SI unit Pa) with crack growth at  $T=0$  timesteps, 20 timesteps, 30 timesteps, and 50 timesteps for three equidistant fractures, with smaller initial middle-fracture length.**

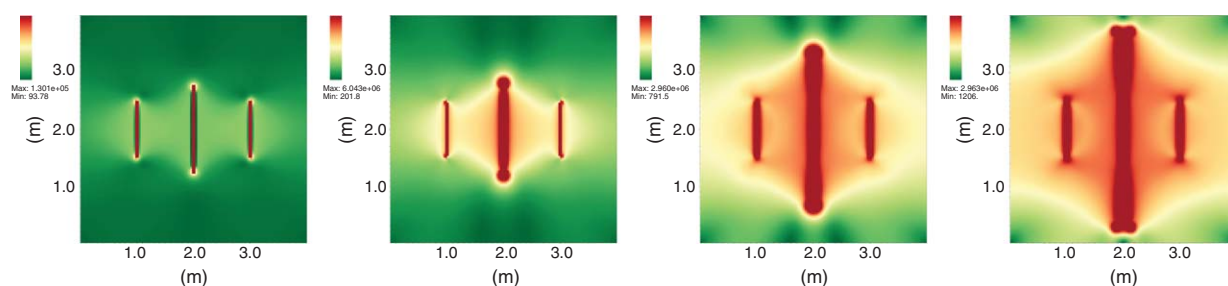


**Fig. 26—Stress-field variation (displayed in the SI unit Pa) with crack growth at  $T=5$  timesteps, 10 timesteps, 20 timesteps, and 30 timesteps for three equidistant fractures, with longer initial middle-fracture length.**



Porosity ( $\phi$ )	0.15–0.22	$K_x \neq K_y = K_z$	0–3800 md
Water compressibility ( $c_w$ )	$10^{-7}$ psi $^{-1}$	Oil compressibility ( $c_o$ )	$10^{-4}$ psi $^{-1}$
Water density ( $\rho_w$ )	62.4 lbm/ft $^3$	Oil density ( $\rho_o$ )	56 lbm/ft $^3$
Water viscosity ( $\nu_w$ )	1 cp	Oil viscosity ( $\nu_o$ )	2 cp
Initial water saturation ( $S_w$ )	0.31	Initial pressure ( $p$ )	1,500 psi

Table 2—Reservoir properties: multistage fractures.

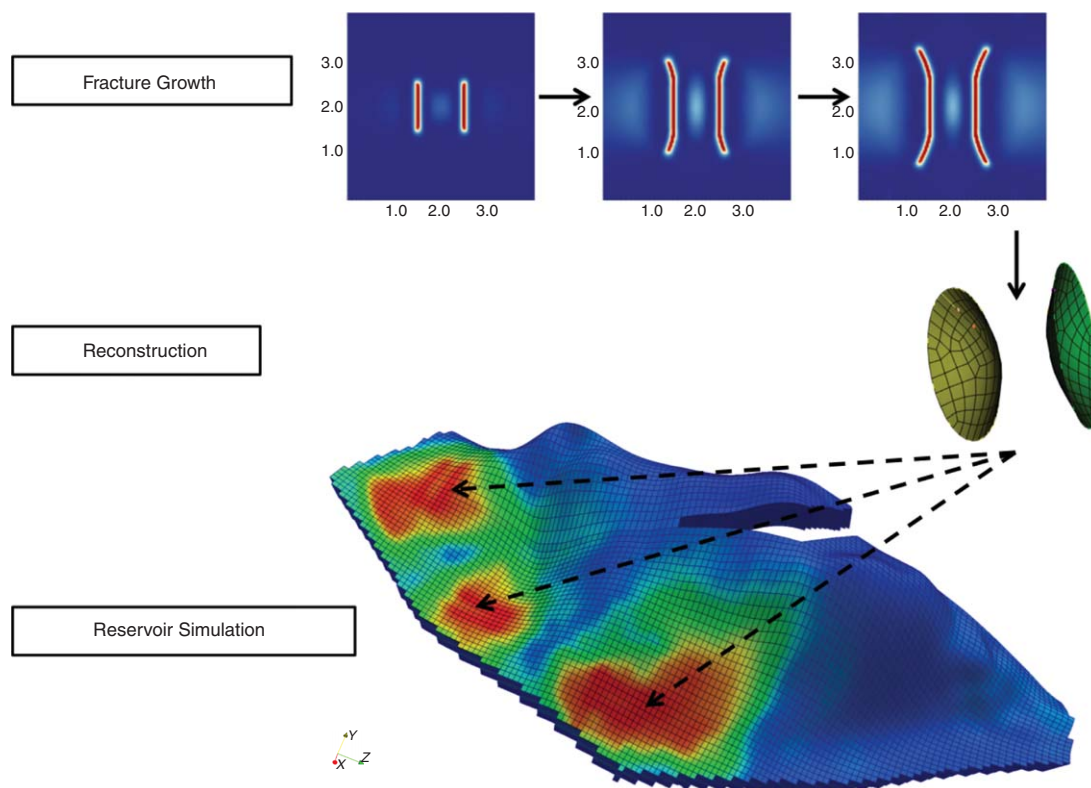


Fig. 27—Fractured reservoir management: integrating from production stimulation to long-term predictions.

fractured wells reduces the number of injection wells while improving sweep efficiency. The phase-field fracture-propagation model, followed by production evaluation of reservoir, allows us to develop an intuitive understanding of recovery predictions and serves as a decision-making tool for design, evaluation, and long-term field developments. Although not restrictive, for the sake of simplicity, we consider the fracture pattern, as shown in Fig. 10. The geometry information from the phase-field fracture-propagation model is post-processed and adapted to obtain a coarser mesh while maintaining mesh quality. This reduces timestep-size restrictions and numerical errors associated with mesh elements. Fig. 5 shows the reconstructed, coarse, structured fracture mesh with quadrilateral (hexahedral in 3D) elements. This fracture pattern is integrated with a wellbore model and is used as a frac-

tured-well model in our reservoir simulator IPARS (integrated parallel accurate reservoir simulator). The reader is referred to Singh et al. (2014) for more details on the fractured poroelastic reservoir-flow modeling.

Table 2 provides material and fluid properties required for solving flow and geomechanics. The values presented in the table provide typical values used for this simulation run. Fig. 28 (left) shows the fractured Brugge field geometry with 20 bottomhole-pressure-specified production wells at 1,000 psi. Here, a pressure profile after 2 days is used to aid in visualizing the location of the fractured injection wells. The three red regions show the hydraulically fractured injection wells with a bottomhole-pressure specification of 2600 psi. The original Brugge field case is shown in Fig. 28 (right) with 30 bottomhole-pressure-specified wells with 10

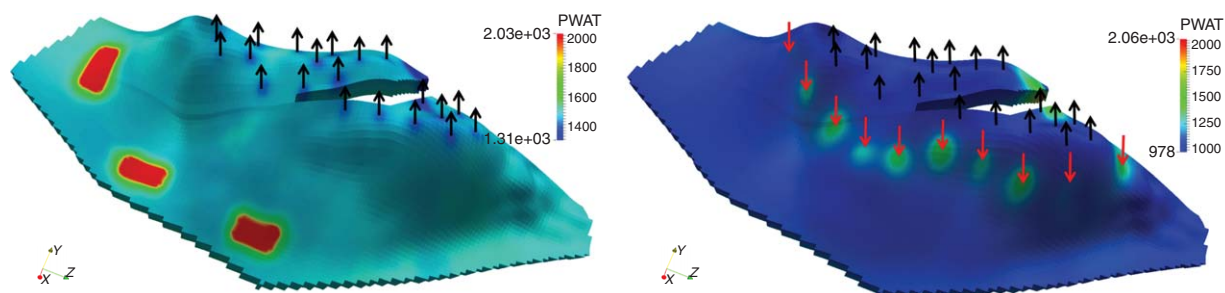


Fig. 28—Fractured reservoir management: integrating from production stimulation to long-term predictions.

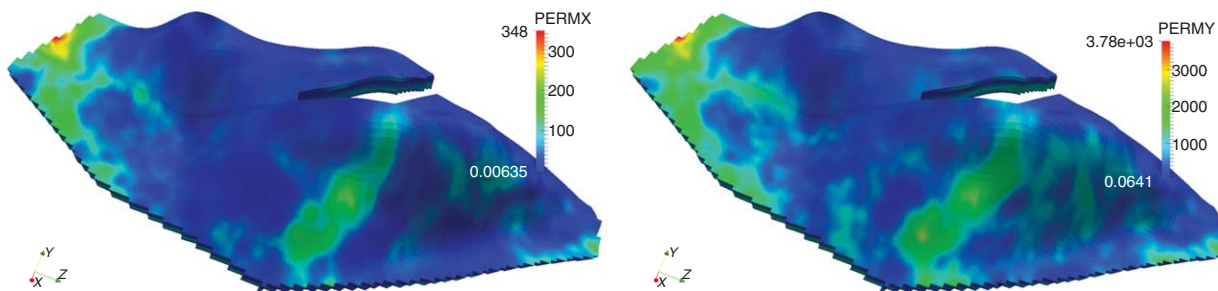


Fig. 29—X-direction (left) and Y-direction (right) permeability fields (md).

injectors at 2600 psi and 20 producers at 1000 psi in which injectors are at a higher elevation compared with the producers. The distorted reservoir geometry and fractures are captured with  $9 \times 48 \times 139$  general hexahedral elements and then discretized with an MFME scheme (Ingram et al. 2010). Fig. 29 displays permeability fields in the X (left) and Y (right) directions. The Z-direction permeability is equal to the Y-direction permeability.

Fig. 30 shows pressure (left) and saturation (right) profiles at the end of 1,000 days. The fractured injection wells are placed at greater depths compared with production wells so that the gravity assists in oil recovery. A comparison between the pressure and saturation profiles for the two cases shows that a lower number of fractured wells is required for improved sweep efficiencies compared with conventional wells. The pressure distribution and permeability field in Figs. 29 through 30 are measured in psi and md (field units), respectively.

## Conclusions

In this work, we first presented a fracture-propagation model and its numerical solution scheme for treating slickwater hydraulic fracturing on the basis of a phase-field approach. This adequately describes crack propagation and associated pressure variation during growth. First, this phase-field model is used to compute various fracture-propagation scenarios in two and three dimensions and crack growth in an anisotropic, heterogeneous, poroelastic medium. In particular, the pressure profile shows a buildup until a critical energy rate is reached resulting in fracture growth. Second, we successfully coupled this phase-field approach with a reservoir simulator. The integration is based on a computationally efficient one-way coupling that allows the use of the phase-field

approach as a preprocessor step. With our proposed approach, we are able to simulate hydraulic fracturing and production stages. One can also achieve an extension to black-oil and compositional models for the reservoir-flow description.

## Nomenclature

- $c$  = fluid compressibility
- $C$  = fracture domain
- $e(u)$  = strain tensor
- $E(u, C)$  = energy functional
- $g$  = acceleration caused by gravity
- $G_c$  = critical energy-release rate
- $\mathcal{H}^{d-1}(C)$  = length (2D) or surface area (3D) of fracture, Hausdorff measure
- $I$  = identity tensor
- $K_{R,F}$  = absolute permeability for the reservoir or fracture
- $M$  = Biot parameter
- $p^0$  = reference pressure
- $p_{R,F}$  = fluid pressure in the reservoir or fracture
- $q_{F,R}$  = source/sink for fracture (F) or reservoir (R)
- $q^L$  = fracture-leakage term
- $t^n$  = timestep
- $T_F$  = Terzaghi time
- $u$  = displacement vector
- $v$  = fluid-velocity vector
- $w(u)$  = fracture aperture or width
- $\chi_{f,s}$  = indicator variable to determine fracture or reservoir region
- $\Omega$  = reservoir domain

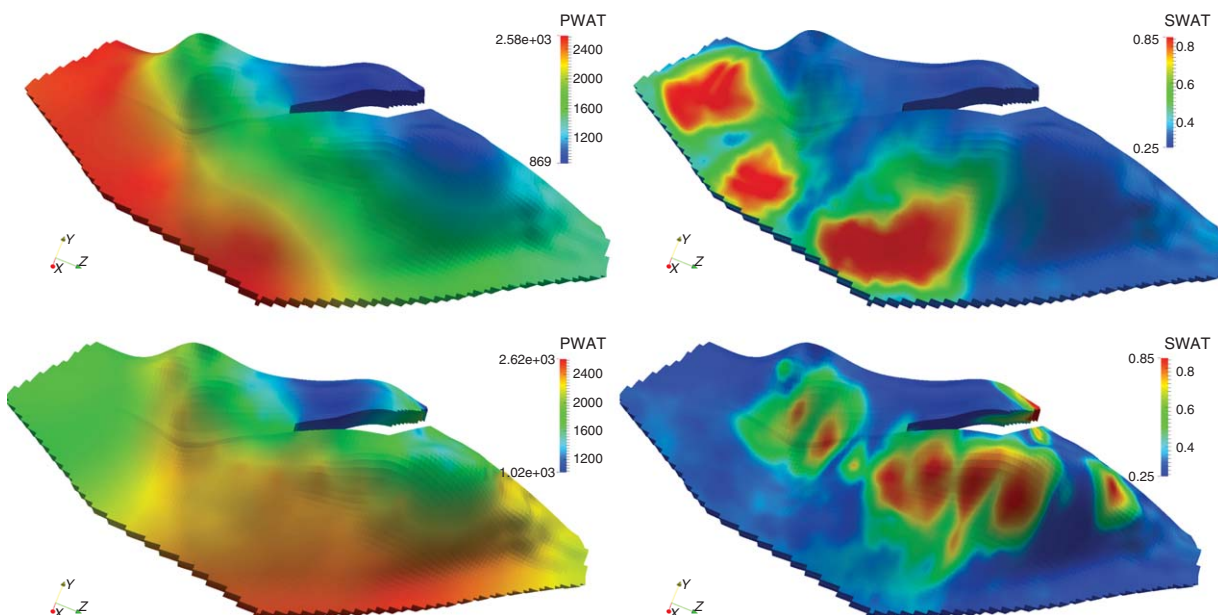


Fig. 30—Pressure (psi) (left) and saturation (right) profiles after 1,000 days for fractured (top) and original (bottom) Brugge field cases.

$\Delta t$  = timestep size  
 $\sigma_E$  = elastic stress tensor  
 $\sigma$  = total stress  
 $\bar{\sigma}$  = mean stress  
 $\alpha_B$  = Biot coefficient  
 $\mu, \lambda$  = Lamé parameters  
 $\nu$  = fluid viscosity  
 $\phi$  = phase-field variable  
 $\tilde{\phi}$  = linear extrapolation in time of the phase-field variable  
 $\phi_+$  = positive part of the phase-field variable  
 $\phi$  = porosity  
 $\phi^0$  = porosity at reference state  
 $\kappa, \varepsilon$  = regularization parameters  
 $\gamma$  = penalization parameter  
 $\Xi$  = augmented Lagrangian function

## Acknowledgments

This research was funded by ConocoPhillips grant UTA10-000444, Department of Energy grant ER25617, Saudi Aramco grant UTA11-000320, and Statoil grant UTA13-000884. In addition, the first author has been supported partially by an Institute for Computational Sciences and Engineering (ICES) post-doctoral fellowship and a Humboldt Feodor Lynen fellowship, and is currently employed by RICAM, an institute funded by the Austrian Academy of Sciences. The authors would like to express their sincere thanks for the funding.

## References

- Abass, H., Soliman, M., Tahini, A. et al. 2009. Oriented fracturing: A New Technique to Hydraulically Fracture an Openhole Horizontal Well. In *Proc.*, SPE Annual Technical Conference and Exhibition, New Orleans, SPE-124483-MS. <http://dx.doi.org/10.2118/124483-MS>.
- Ambrosio, L. and Tortorelli, V. 1990. Approximation of Functionals Depending on Jumps by Elliptic Functionals via Gamma-Convergence. *Communications on Pure and Applied Mathematics* **43** (8): 999–1036. <http://dx.doi.org/10.1002/cpa.3160430805>.
- Ambrosio, L. and Tortorelli, V. 1992. On the Approximation of Free-Discontinuity Problems. *Boll. Un. Mat. Ital.* **6-B**: 105–123.
- Babuska, I. and Melenk, J. 1997. The Partition of Unity Method. *The Int. J. Numer. Methods Engrg.* **40**: 727–758. [http://dx.doi.org/10.1002/\(SICI\)1097-0207\(19970228\)40:4<727::AID-NME86>3.0.CO;2-N](http://dx.doi.org/10.1002/(SICI)1097-0207(19970228)40:4<727::AID-NME86>3.0.CO;2-N).
- Babuska, I. and Banerjee, U. 2012. Stable Generalized Finite Element Method (SGFEM). *Comput. Methods Appl. Mech. Engrg.* **201–204**: 91–111. <http://dx.doi.org/10.1016/j.cma.201109.012>.
- Barenblatt, G. I. 1962. The Mathematical Theory of Equilibrium Cracks in Brittle Fracture. *Advances in Applied Mechanics* **7** (7): 55–129. [http://dx.doi.org/10.1016/s0065-2156\(08\)70121-2](http://dx.doi.org/10.1016/s0065-2156(08)70121-2).
- Biot, M. 1941a. Consolidation Settlement Under a Rectangular Load Distribution. *J. Appl. Phys.* **12** (5): 426–430. <http://dx.doi.org/10.1063/1.1712921>.
- Biot, M. 1941b. General Theory of Three-Dimensional Consolidation. *J. Appl. Phys.* **12** (2): 155–164. <http://dx.doi.org/10.1063/1.1712886>.
- Biot, M. 1955. Theory of Elasticity and Consolidation for a Porous Anisotropic Solid. *J. Appl. Phys.* **26**: 182–185. <http://dx.doi.org/10.1063/1.1721956>.
- Bourdin, B., Chukwudozie, C., and Yoshioka, K. 2012. A Variational Approach to the Numerical Simulation of Hydraulic Fracturing. Presented at the SPE Annual Technical Conference and Exhibition, San Antonio, Texas, USA, 8–10 October. SPE-159154-MS. <http://dx.doi.org/10.2118/159154-MS>.
- Bourdin, B., Francfort, G., and Marigo, J.-J. 2000. Numerical Experiments in Revisited Brittle Fracture. *J. Mech. Phys. Solids* **48** (4): 797–826. [http://dx.doi.org/10.1016/S0022-5096\(99\)00028-9](http://dx.doi.org/10.1016/S0022-5096(99)00028-9).
- Bourdin, B., Francfort, G., and Marigo, J.-J. 2008. The Variational Approach to Fracture. *J. Elasticity* **91** (1–3): 1–148. <http://dx.doi.org/10.1007/s10659-007-9107-3>.
- Carter, E. 1957. *Optimum Fluid Characteristics for Fracture Extension*. Drilling and Production Practices: American Petroleum Institute.
- Castonguay, S., Mear, M., Dean, R. et al. 2013. Predictions of the Growth of Multiple Interacting Hydraulic Fractures in Three Dimensions. Presented at the SPE Annual Technical Conference and Exhibition, New Orleans, 30 September–2 October. SPE-166259-MS. <http://dx.doi.org/10.2118/166259-MS>.
- Chen, H.-Y., Teufel, L., and Lee, R. 1995. Coupled Fluid Flow and Geomechanics in Reservoir Study—I. Theory and Governing Equations. Presented at the SPE Annual Technical Conference and Exhibition, Dallas, 22–25 October. SPE-30752-MS. <http://dx.doi.org/10.2118/30752-MS>.
- Chen, Z., Bungler, A., Zhang, X. et al. 2009. Cohesive Zone Finite Element-Based Modeling of Hydraulic Fractures. *Acta Mechanica Sinica* **22**: 443–452. [http://dx.doi.org/10.1016/S0894-9166\(09\)60295-0](http://dx.doi.org/10.1016/S0894-9166(09)60295-0).
- Chen, C., Wang, Y., and Li, G. 2010. Closed-Loop Reservoir Management on the Brugge Test Case. *Comput. Geosci.* **14**: 691–703. <http://dx.doi.org/10.1007/s10596-010-9181-7>.
- Coussy, O. 1995. *Mechanics of Porous Continua*. Hoboken, New Jersey: John Wiley & Sons.
- Coussy, O. 2004. *Poromechanics*. Hoboken, New Jersey: John Wiley & Sons.
- Crouch, S. 1976. Solution of Plane Elastic Problem by the Displacements Discontinuity Method. I. Infinite Body Solution. *Int. J. Num. Meth. in Eng.* **10**: 301–343. <http://dx.doi.org/10.1002/nme.1620100206>.
- de Borst, R., Rethoré, J., and Abellan, M. 2006. A Numerical Approach for Arbitrary Cracks in a Fluid-Saturated Porous Medium. *Arch. Appl. Mech.* **75**: 595–606. <http://dx.doi.org/10.1007/s00419-006-0023-y>.
- Dean, R. H. and Schmidt, J. 2008. Hydraulic Fracture Predictions With a Fully Coupled Geomechanical Reservoir Simulator. Presented at the SPE Annual Technical Conference and Exhibition, Denver, 21–24 September. SPE-116470-MS. <http://dx.doi.org/10.2118/116470-MS>.
- Dean, R. and Schmidt, J. 2009. Hydraulic-Fracture Predictions With a Fully Coupled Geomechanical Reservoir Simulator. *SPE J.* **14** (4): 707–714. SPE-116470-PA. <http://dx.doi.org/10.2118/116470-PA>.
- Fisher, M., Heinze, J., Harris, C. et al. 2004. Optimizing Horizontal Completion Techniques in The Barnett Shale Using Microseismic Fracture Mapping. In *Proc.*, SPE Annual Technology Conference and Exhibition, Houston, USA, 26–29 September. SPE-90051-MS. <http://dx.doi.org/10.2118/90051-MS>.
- Francfort, G. A. and Marigo, J.-J. 1998. Revisiting Brittle Fracture As an Energy Minimization Problem. *J. Mech. Phys. Solids* **46** (8): 1319–1342. [http://dx.doi.org/10.1016/S0022-5096\(98\)00034-9](http://dx.doi.org/10.1016/S0022-5096(98)00034-9).
- Gai, X. 2004. *A Coupled Geomechanics and Reservoir Flow Model on Parallel Computers*. PhD thesis, The University of Texas at Austin.
- Germanovich, L., Ring, L., Astakhov, D. et al. 1997. Hydraulic Fracture With Multiple Segments II: Modeling. *Int. J. Rock Mech. Min. Sci.* **34** (3–4): 98.e1–98.e15. [http://dx.doi.org/10.1016/S1365-1609\(97\)00079-8](http://dx.doi.org/10.1016/S1365-1609(97)00079-8).
- Gordeliy, E. and Peirce, A. 2013a. Coupling Schemes for Modeling Hydraulic Fracture Propagation Using the XFEM. *Comp. Meth. Appl. Mech. Engrg.* **253**: 305–322. <http://dx.doi.org/10.1016/j.cma.2012.08.017>.
- Gordeliy, E. and Peirce, A. 2013b. Implicit Level Set Schemes for Modeling Hydraulic Fractures Using the Xfem. *Comp. Meth. Appl. Mech. Engrg.* **266**: 125–143. <http://dx.doi.org/10.1016/j.cma.2013.07.016>.
- Griffith, A. A. 1921. The Phenomena of Rupture and Flow in Solids. *Philosophical Trans. of the Royal Society of London. Series A, Containing Papers of a Mathematical or Physical Character*, **221**: 163–198. <http://dx.doi.org/10.1098/rsta.1921.0006>.
- Gupta, P. and Duarte, C. A. 2014. Simulation of Non-Planar Three-Dimensional Hydraulic Fracture Propagation. *International Journal for Numerical and Analytical Methods in Geomechanics* **38** (13): 1397–1430. <http://dx.doi.org/10.1002/nag.2305>.
- Heister, T., Wheeler, M. F., and Wick, T. 2015. A Primal-Dual Active Set Method and Predictor-Corrector Mesh Adaptivity for Computing Fracture Propagation Using a Phase-Field Approach. *Comput. Methods Appl. Mech. Engrg.* **290**: 466–495. <http://dx.doi.org/10.1016/j.cma.2015.03.009>.
- Ingram, R., Wheeler, M. F., and Yotov, I. 2010. A Multipoint Flux Mixed Finite Element Method on Hexahedra. *SIAM Journal on Numerical Analysis* **48** (4): 1281–1312. <http://dx.doi.org/10.1137/090766176>.
- Irwin, G. 1958. *Elastizität und plastizität. Handbuch der Physik*, S. Flügge, ed., Bd. 6.
- Katiyar, A., Foster, J. T., Ouchi, H. et al. 2014. A Peridynamic Formulation of Pressure Driven Convective Fluid Transport in Porous Media.



- Journal of Computational Physics* **261**: 209–229. <http://dx.doi.org/10.1016/j.jcp.2013.12.039>.
- Kim, J., Tchelepi, H. A., and Juanes, R. 2009. Stability, Accuracy, and Efficiency of Sequential Methods for Coupled Flow and Geomechanics. *SPE J.* **16** (2): 249–262. SPE-119084-PA. <http://dx.doi.org/10.2118/119084-PA>.
- Kresse, O., Weng, X., Gu, H. et al. 2013. Numerical Modeling of Hydraulic Fracture Interaction in Complex Naturally Fractured Formations. *Rock Mech. Rock Eng.* **46** (3): 555–568. <http://dx.doi.org/10.1007/s00603-012-0359-2>.
- Kreyszig, E. 2010. *Advanced Engineering Mathematics*. Hoboken, New Jersey: John Wiley & Sons.
- Ladyzhenskaja, O., Solonnikov, V., and Uralceva, N. 1968. *Linear and Quasi-Linear Equations of Parabolic Type*. Translations of mathematical monographs, AMS Vol. 23.
- Lecampion, B. 2009. An Extended Finite Element Method for Hydraulic Fracture Problems. *Communications in Numerical Methods in Engineering* **25** (2): 121–133. <http://dx.doi.org/10.1002/cnm.1111>.
- Liu, R. 2004. *Discontinuous Galerkin Finite Element Solution for Poromechanics*. PhD thesis, The University of Texas at Austin.
- Lujun, J., Settari, A., and Sullivan, R. B. 2007. A Novel Hydraulic Fracturing Model Fully Coupled With Geomechanics and Reservoir Simulator. Paper presented at the SPE Annual Technical Conference and Exhibition, Anaheim, California, USA, 11–14 November. SPE-110845-MS. <http://dx.doi.org/10.2118/110845-MS>.
- Meyer, B. and Bazan, L. 2011. A Discrete Fracture Network Model for Hydraulically Induced Fractures-Theory, Parametric and Case Studies. In *Proc.*, SPE Hydraulic Fracturing Technology Conference and Exhibition. The Woodlands, Texas, USA, 24–26 January. SPE-140514-MS. <http://dx.doi.org/10.2118/140514-MS>.
- Miehe, C., Welschinger, F., and Hofacker, M. 2010. Thermodynamically Consistent Phase-Field Models of Fracture: Variational Principles and Multi-Field FE Implementations. *International Journal of Numerical Methods in Engineering* **83**: 1273–1311. <http://dx.doi.org/10.1002/nme.2861>.
- Mikelić, A. and Wheeler, M. F. 2013. Convergence of Iterative Coupling for Coupled Flow and Geomechanics. *Comput. Geosci.* **17** (3): 455–461. <http://dx.doi.org/10.1007/s10596-012-9318-y>.
- Mikelić, A., Wheeler, M., and Wick, T. 2013. A Phase-Field Approach to the Fluid Filled Fracture Surrounded by a Poroelastic Medium. ICES-Preprint 13-15.
- Mikelić, A., Wang, B., and Wheeler, M. F. 2014. Numerical Convergence Study of Iterative Coupling for Coupled Flow and Geomechanics. *Comput. Geosci.* **18** (3–4): 325–341. <http://dx.doi.org/10.1007/s10596-013-9393-8>.
- Mikelić, A., Wheeler, M., and Wick, T. 2015a. A Phase-Field Method for Propagating Fluid-Filled Fractures Coupled to a Surrounding Porous Medium. *SIAM Multiscale Modeling and Simulation* **13** (1): 367–398. <http://dx.doi.org/10.1137/140967118>.
- Mikelić, A., Wheeler, M. F., and Wick, T. 2015b. A Quasi-Static Phase-Field Approach to Pressurized Fractures. *Nonlinearity* **28** (5): 1371–1399. <http://dx.doi.org/10.1088/0951-7715/28/5/1371>.
- Moes, N., Dolbow, J., and Belytschko, T. 1999. A Finite Element Method for Crack Growth Without Remeshing. *Int. J. Numer. Methods Engrg.* **46**: 131–150. [http://dx.doi.org/10.1002/\(SICI\)1097-0207\(19990910\)46:1<131::AID-NME726>3.0.CO;2-J](http://dx.doi.org/10.1002/(SICI)1097-0207(19990910)46:1<131::AID-NME726>3.0.CO;2-J).
- Olson, J. 2008. Multi-Fracture Propagation Modeling: Applications to Hydraulic Fracturing in Shales and Tight Gas Sands. In *Proc.*, 42nd US Rock Mechanics Symposium, San Francisco, 29 June–2 July. Paper No. 08-327.
- Peaceman, D. W. 1978. Interpretation of Well-Block Pressures in Numerical Reservoir Simulation. *SPE J.* **18** (3): 183–194. SPE-6893-PA. <http://dx.doi.org/10.2118/6893-PA>.
- Peirce, A. and Detournay, E. 2008. An Implicit Level Set Method for Modeling Hydraulically Driven Fractures. *Comput. Meth. Appl. Mech. Engrg.* **197**: 2858–2885. <http://dx.doi.org/10.1016/j.cma.2008.01.013>.
- Peters, E., Arts, R., Brouwer, G. et al. 2009. Results of the Brugge Benchmark Study for Flooding Optimization and History Matching. Presented at the SPE Reservoir Simulation Symposium, The Woodlands, Texas, 2–4 February. SPE 119094-MS. <http://dx.doi.org/10.2118/119094-MS>.
- Pham, K., Amor, H., Marigo, J.-J. et al. 2011. Gradient Damage Models and Their Use to Approximate Brittle Fracture. *Int. J. of Damage Mech.* **20** (4): 618–652. <http://dx.doi.org/10.1177/1056789510386852>.
- Ren, Q., Dong, Y., and Yu, T. 2009. Numerical Modeling of Concrete Hydraulic With Extended Finite Element Method. *Science in China Series E: Technological Science* **52** (3): 559–565. <http://dx.doi.org/10.1007/s11431-009-0058-8>.
- Roussel, N. P. and Sharma, M. M. 2011. Optimizing Fracture Spacing and Sequencing in Horizontal-Well Fracturing. *SPE Prod & Oper* **26** (2): 173–184. SPE-127986-PA. <http://dx.doi.org/10.2118/127986-PA>.
- Roussel, N. P., Manchanda, R., and Sharma, M. M. 2012. Implications of Fracturing Pressure Data Recorded During a Horizontal Completion on Stage Spacing Design. In *Proc.*, SPE Hydraulic Fracturing Technology Conference and Exhibition, The Woodlands, Texas, USA, 6–8 February. SPE-152631-MS. <http://dx.doi.org/10.2118/152631-MS>.
- Savitski, A. and Detournay, E. 2002. Propagation of a Penny-Shaped Fluid-Driven Fracture in an Impermeable Rock: Asymptotic Solutions. *International Journal of Solids and Structures* **39**: 6311–6337. [http://dx.doi.org/10.1016/S0020-7683\(02\)00492-4](http://dx.doi.org/10.1016/S0020-7683(02)00492-4).
- Secchi, S. and Schrefler, B. A. 2012. A Method for 3D Hydraulic Fracturing Simulation. *Int. J. Fract.* **178**: 245–258. <http://dx.doi.org/10.1007/s10704-012-9742-y>.
- Sesetty, V. and Ghassemi, A. 2013. Numerical Simulation of Sequential and Simultaneous Hydraulic Fracturing. In *Effective and Sustainable Hydraulic Fracturing*, A. P. Bunger, J. McLennan, and R. G. Jeffrey, ed., Chapter 33. Rijeka, Croatia: Intech.
- Settari, A. and Walters, D. A. 2001. Advances in Coupled Geomechanical and Reservoir Modeling With Applications to Reservoir Compaction. *SPE J.* **6** (3): 334–342. SPE-74142-PA. <http://dx.doi.org/10.2118/74142-PA>.
- Silling, S. A. 2000. Reformulation of Elasticity Theory for Discontinuities and Long-Range Forces. *Journal of the Mechanics and Physics of Solids* **48** (1): 175–209. [http://dx.doi.org/10.1016/S0022-5096\(99\)00029-0](http://dx.doi.org/10.1016/S0022-5096(99)00029-0).
- Singh, G., Wick, T., Wheeler, M. et al. 2014. Impact of Accurate Fractured Reservoir Flow Modeling on Recovery Predictions. Presented at the SPE Hydraulic Fracturing Technology Conference, The Woodlands, Texas, USA, 4–6 February. SPE-168630-MS. <http://dx.doi.org/10.2118/168630-MS>.
- Sneddon, I. N. and Lowengrub, M. 1969. *Crack Problems in the Classical Theory of Elasticity*. SIAM series in Applied Mathematics. Hoboken, New Jersey: John Wiley & Sons.
- Taleghani, A. 2009. *Analysis of Hydraulic Fracture Propagation in Fractured Reservoirs: An Improved Model for the Interaction Between Induced and Natural Fractures*. PhD thesis, The University of Texas at Austin.
- Wheeler, M., Wick, T., and Wollner, W. 2014. An Augmented-Lagrangian Method for the Phase-Field Approach for Pressurized Fractures. *Comp. Meth. Appl. Mech. Engrg.* **271**: 69–85. <http://dx.doi.org/10.1016/j.cma.2013.12.005>.
- Wick, T. 2015. Dual-Weighted Residual Adaptivity for Phase-Field Fracture Propagation. Accepted for publication in the online journal PAMM—Proc. of Applied Mathematics and Mechanics, Vol. 15 (November 2015).
- Xu, X. and Needleman, A. 1994. Numerical Simulations of Fast Crack Growth in Brittle Solids. *Journal of the Mechanics and Physics of Solids* **42**: 1397–1434. [http://dx.doi.org/10.1016/0022-5096\(94\)90003-5](http://dx.doi.org/10.1016/0022-5096(94)90003-5).
- Zhang, X., Detournay, E., and Jeffrey, R. 2002. Propagation of a Penny-Shaped Hydraulic Fracture Parallel to the Free-Surface of an Elastic Half-Space. *International Journal of Fracture* **115** (2): 125–158. <http://dx.doi.org/10.1023/A:1016345906315>.
- Zhang, X., Jeffrey, R., and Thiercelin, M. 2007. Deflection and Propagation of Fluid-Driven Fractures at Frictional Bedding Interfaces: A Numerical Investigation. *J. Struct. Geol.* **29** (3): 396–410. <http://dx.doi.org/10.1016/j.jsg.2006.09.013>.

**Gurpreet Singh** is a post-doctoral research fellow at the Center for Subsurface Modeling, the University of Texas at Austin. He holds MS and PhD degrees in petroleum engineering from the Pennsylvania State University and the University of Texas at Austin, respectively, and a BS degree in chemical engineering

from G. G. S. Indraprastha University, India. Singh's research interests include flow and reactive transport in porous media, phase behavior, and compositional flow modeling.

**Mary F. Wheeler** is a professor in the departments of Mathematics, Petroleum and Geosystems Engineering, and Aerospace Engineering and Engineering Mechanics at the University of Texas at Austin. She is the director of the Center for Subsurface Modeling in the Institute for Computational Engineering and Sciences at that university. Wheeler's research interests include the numerical solution of partial-differential-

equation systems with applications to the modeling of subsurface and surface flows and parallel computation.

**Thomas Wick** is a research scientist at the Austrian Academy of Sciences and is currently also a visiting professor at the Technical University of Munich. Previously, he worked 2 years as a post-doctoral fellow at the University of Texas at Austin. Wick's research interests include phase-field fracture modeling in poroelasticity, fluid/structure interaction, and computational fluid and solid mechanics. He holds a PhD degree in applied mathematics from Heidelberg University, Germany.